nature medicine

ARTICLES

https://doi.org/10.1038/s41591-021-01663-5

Check for updates

Activity-dependent spinal cord neuromodulation rapidly restores trunk and leg motor functions after complete paralysis

Andreas Rowald[1,2,3,27], Salif Komi[1,2,3,27], Robin Demesmaeker[1,2,3,27], Edeny Baaklini[1,2,3], Sergio Daniel Hernandez-Charpak[1,2,3], Edoardo Paoles[4], Hazael Montanaro[5,6], Antonino Cassara[5], Fabio Becce[7], Bryn Lloyd[5], Taylor Newton[5], Jimmy Ravier[1,2,3], Nawal Kinany[1,8,9], Marina D'Ercole[4], Aurélie Paley[2,3], Nicolas Hankov[1,2,3], Camille Varescon[1,2,3], Laura McCracken[1,2,3], Molywan Vat[2,3], Miroslav Caban[4,8], Anne Watrin[4], Charlotte Jacquet[4], Léa Bole-Feysot[1,2,3], Cathal Harte[1,2,3], Henri Lorach[1,2,3], Andrea Galvez[1,2,3], Manon Tschopp[2], Natacha Herrmann[2], Moïra Wacker[2], Lionel Geernaert[2], Isabelle Fodor[2], Valentin Radevich[2], Katrien Van Den Keybus[2], Grégoire Eberle[2], Etienne Pralong[10], Maxime Roulet[3,10], Jean-Baptiste Ledoux[7,11], Eleonora Fornari[7,11], Stefano Mandija[12], Loan Mattera[13], Roberto Martuzzi[13], Bruno Nazarian[14], Stefan Benkler[5], Simone Callegari[15], Nathan Greiner[1,2,3], Benjamin Fuhrer[1,2], Martijn Froeling[12], Nik Buse[16], Tim Denison[16,17], Rik Buschman[16], Christian Wende[18], Damien Ganty[4], Jurriaan Bakker[4], Vincent Delattre[4], Hendrik Lambert[4], Karen Minassian[19], Cornelis A. T. van den Berg[12], Anne Kavounoudias[20], Silvestro Micera[9,21], Dimitri Van De Ville[8,22], Quentin Barraud[1,2,3], Erkan Kurt[23], Niels Kuster[5,6,15], Esra Neufeld[5,6,15], Marco Capogrosso[1,24,25], Leonie Asboth[1,2,3], Fabien B. Wagner[1,2,3,26,28], Jocelyne Bloch[1,2,3,10,28] ✉ and Grégoire Courtine[1,2,3,10,28] ✉

Epidural electrical stimulation (EES) targeting the dorsal roots of lumbosacral segments restores walking in people with spinal cord injury (SCI). However, EES is delivered with multielectrode paddle leads that were originally designed to target the dorsal column of the spinal cord. Here, we hypothesized that an arrangement of electrodes targeting the ensemble of dorsal roots involved in leg and trunk movements would result in superior efficacy, restoring more diverse motor activities after the most severe SCI. To test this hypothesis, we established a computational framework that informed the optimal arrangement of electrodes on a new paddle lead and guided its neurosurgical positioning. We also developed software supporting the rapid configuration of activity-specific stimulation programs that reproduced the natural activation of motor neurons underlying each activity. We tested these neurotechnologies in three individuals with complete sensorimotor paralysis as part of an ongoing clinical trial (www.clinicaltrials.gov identifier NCT02936453). Within a single day, activity-specific stimulation programs enabled these three individuals to stand, walk, cycle, swim and control trunk movements. Neurorehabilitation mediated sufficient improvement to restore these activities in community settings, opening a realistic path to support everyday mobility with EES in people with SCI.

Three decades of preclinical[1–6] and clinical[7–16] research have shown that EES applied over the lumbosacral spinal cord can restore walking after SCI. A subset of the treated individuals with motor complete paralysis can even walk overground with EES after many months of intense training when assisted by multiple physical therapists[7,10]. However, translating these isolated proofs of concept into a commonly available therapy requires neurotechnologies that not only enable the rapid recovery of numerous motor activities with limited human resources but also mediate this recovery in every treated individual. Here, we aim to address these challenges.

EES recruits large-diameter afferent fibers at their entrance in the spinal cord through the dorsal roots[12,17–20]. The recruitment of these fibers leads to the activation of motor neurons embedded in the spinal segment innervated by the root wherein these fibers reside[4,8]. Therefore, targeting individual dorsal roots enables the modulation of specific motor neuron ensembles[4,8,21]. This biological principle guided the development of EES programs[4,21–23] that target the individual dorsal roots with a predefined timing to reproduce the natural spatiotemporal activation pattern[24,25] of motor neurons during walking. Compared to continuous EES, these biomimetic stimulation programs have mediated superior recovery of walking after SCI[4,8,12,21].

A full list of affiliations appears at the end of the paper.

EES has been delivered using repurposed neurotechnologies that were initially designed to alleviate pain[7–14]. These neurotechnologies include paddle leads with an arrangement of electrodes that target the dorsal column[26]. Instead, the recovery of motor functions requires targeting the dorsal roots[27]. Moreover, the short length of existing paddle leads limits the number of dorsal roots that can be targeted with EES. Therefore, current neurotechnologies fail to leverage the biological principles through which EES restores movement after SCI.

Here, we designed and fabricated a paddle lead with an arrangement of electrodes that targeted the ensemble of dorsal roots involved in leg and lower-trunk movements. We also established a computational framework combining high-resolution structural and functional imaging to optimize the surgical placement of this lead. Finally, we developed a software to support the rapid configuration of biomimetic stimulation programs.

We aimed to leverage this portfolio of purposed-built neurotechnologies to elaborate activity-dependent biomimetic stimulation programs that address the deficits of individuals presenting with the most severe forms of SCI across a broad range of activities, including the critically important control of the trunk[10,28,29].

Results

Variability of spinal cord topology. Sacral (S1 and S2), lumbar (L1–L5) and low thoracic (T12) dorsal roots project to spinal segments containing motor neurons innervating leg and lower-trunk muscles (Fig. 1a). Therefore, we aimed to identify an arrangement of electrodes that would be suitable to target all of these roots across the human population. We first determined whether the interindividual variability of spinal cord anatomy was compatible with this aim.

Neuroanatomical quantification of 27 spinal cords exposed a pronounced variability of spinal segment lengths, in particular across upper lumbar segments (Fig. 1b). We complemented this survey with an analysis of the tridimensional topology of dorsal roots, because we showed that this topology determines the distribution of EES-induced electric potentials along the roots[30]. To enable this visualization, we optimized structural magnetic resonance imaging (MRI) sequences that increased the tridimensional spatial resolution while enhancing the contrast resolution between the cerebrospinal fluid and spinal cord tissues (Fig. 1c and Extended Data Fig. 1). This contrast enabled the semiautomated conversion of MRI and computed tomography (CT) images into realistic anatomical models of the entire spine (Fig. 1d). This visualization confirmed the pronounced variability in the rostrocaudal distribution of dorsal roots (Fig. 1b). Instead, we found that the widths of the dorsal root entry zones were remarkably consistent (Fig. 1b and Extended Data Fig. 2).

Atlas of spinal cord models. Our pulse generator could accommodate 16 electrodes. Therefore, our challenge was to identify an arrangement of 16 electrodes that accessed the 16 targeted dorsal roots despite the variable topology of the spinal cord. We posited that resolving this challenge would require tradeoffs and that identifying these tradeoffs would be contingent on computational models.

We thus established a pipeline to generate highly realistic computational models of the interactions between EES and the spinal cord. This pipeline leveraged the verified anatomical and biophysical models of the Sim4Life computational life-sciences simulation platform[31] to generate tridimensional finite element models of the spine from CT and MRI scans (Fig. 1 and Extended Data Fig. 1), created models of rootlet bundles and their innervation patterns (Extended Data Fig. 2) and functionalized these geometries with fiber models covering the entire populations of efferent and afferent fibers (Fig. 1f). The physics and neuron electrophysiology solvers of the Sim4Life simulation platform then predicted the probability of recruiting these fibers when delivering EES. These simulations confirmed[19] that EES preferentially recruits large-diameter afferents, because nearly all A fibers were recruited before the depolarization of A fibers (Fig. 1g).

We then used this pipeline to generate a freely available atlas of 15 personalized computational models that provided a resource to study the optimal arrangements of electrode across a large human population.

Optimized electrode arrangement. We reasoned that identifying an optimal arrangement of electrodes would require circumscribing the analysis to the key features that determine the selectivity of EES. We thus focused our analysis on four features (Fig. 2a):

(1) Rostrocaudal distributions: We merged all the spinal cords of the atlas into a unified model that captured the average topology of the human spinal cord. This model informed the optimal length of the paddle. We then distributed the electrodes uniformly along the rostrocaudal direction (Fig. 2b).

(2) Lateral positions to maximize le -right selectivity: Simulations predicted a maximal selectivity with an electrode positioned 2.3 mm lateral to the midline. However, this selectivity declined by 50% with a lateral shift as small as 1 mm. Such deviations are inevitable when a paddle lead is inserted into the irregular spinal canal. Simulations indicated that placing the electrodes at 4.7 mm from the midline would mitigate the impact of potential mediolateral deviations (Fig. 2c).

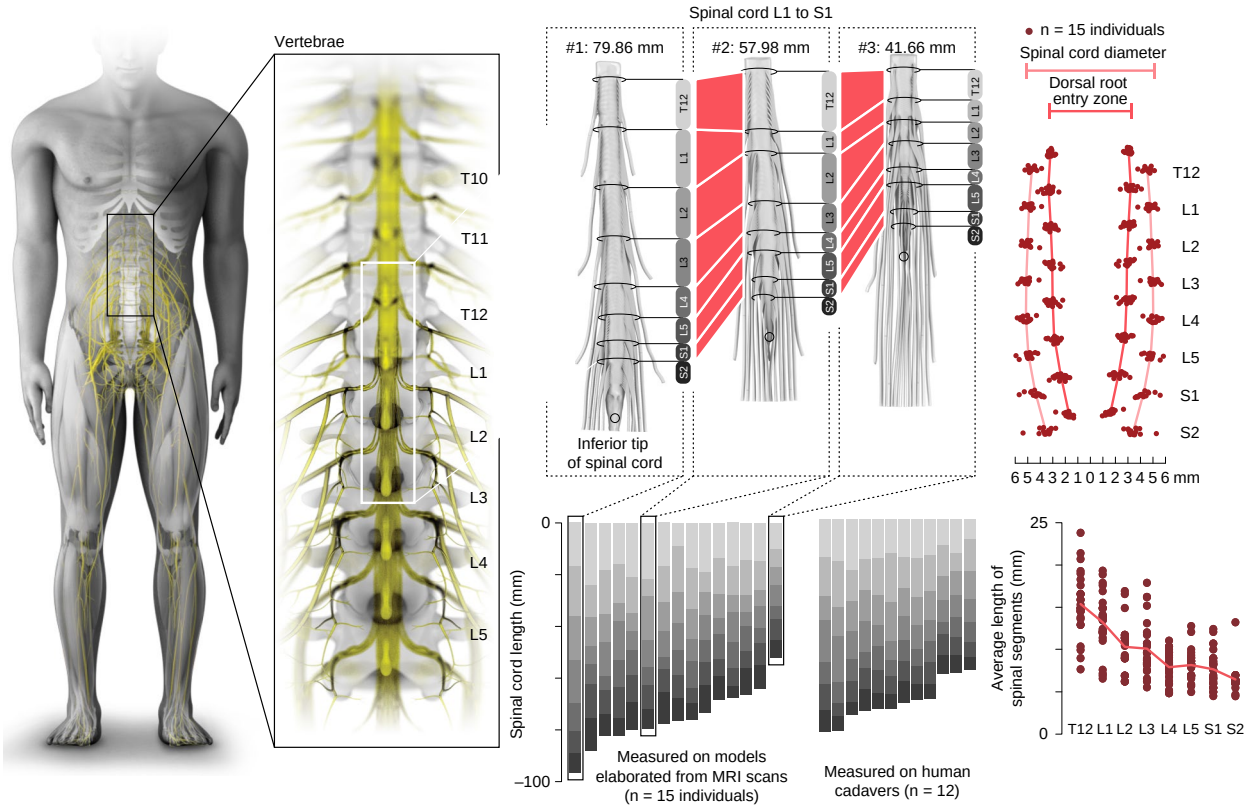
(3) Midline positions to steer current: Simulations showed that increasing the amplitude of EES leads to a proportional recruitment of nontargeted dorsal roots, especially from the contralateral side (Fig. 2d). To minimize this undesired recruitment, we incorporated midline electrodes, as simulations revealed that creating multipolar configurations with lateral and midline electrodes steered the current toward the targeted root while minimizing the recruitment of contralateral roots (Fig. 2d).

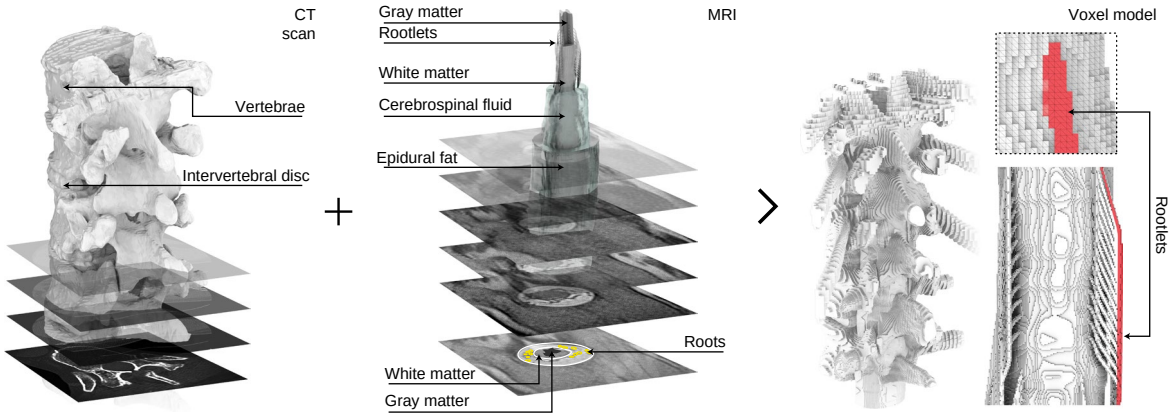
(4) Arrangement for the sacral region: The agglutination of the lumbar rootlets around sacral segments is an impediment to the selective recruitment of the sacral root entry zones (Fig. 2e). Because the somatotopy of the lumbar dorsal rootlet bundles is maintained along the transverse axis of sacral segments, we reasoned that a transverse arrangement of electrodes would rescue this selectivity. Simulations confirmed these considerations (Fig. 2e).

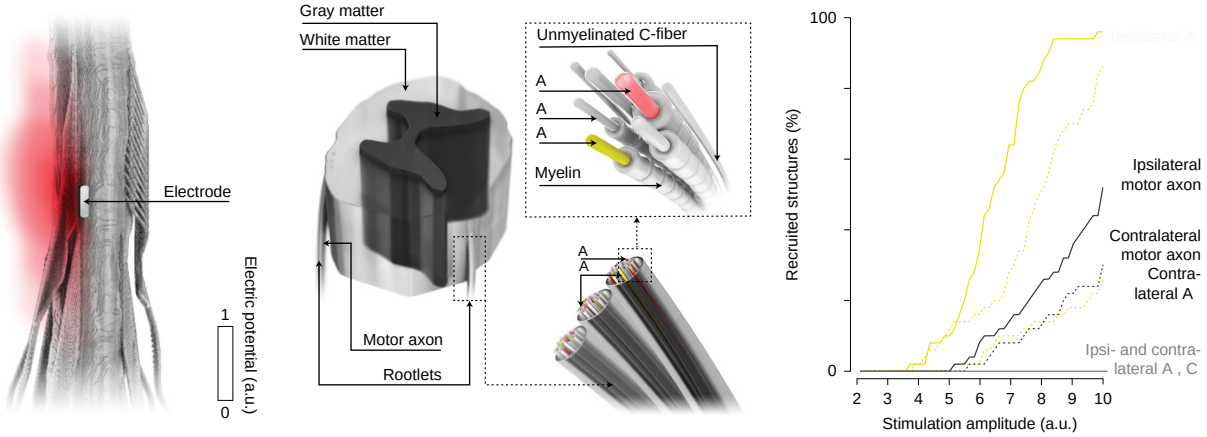
We translated these predictions into an arrangement of 16 electrodes that we accommodated on a new paddle lead fabricated with standard medical-grade processes (Fig. 2f).

Precise preoperative planning. We then evaluated the selectivity of this lead across the 15 computational models. Performances differed widely across individual models (Extended Data Fig. 2), as expected

Fig. 1 | Anatomical quantification and personalizable computational models. a, Human spinal cord, including a visualization of the targeted thoracic, lumbar and sacral dorsal roots. **b**, Spinal cord topology from 27 adult individuals was quantified using MRI/CT scans of 15 healthy volunteers and anatomical measurements of 12 cadavers. Each bar or dot reports measurements from one individual. Three complete anatomical models are shown from individuals with widely different topologies. **c**, Automated framework to elaborate anatomical models of spinal cord tissues from high-resolution MRI and CT images. **d**, Discretization of anatomical models as voxels using rectilinear (structured) gridding. **e**, Distribution of electric potential when delivering one pulse of EES. **f**, Compartmental cable models incorporating the entire range of afferents and efferents are initialized in the rootlets. **g**, Relative recruitment of afferents and efferents when delivering a single pulse of EES with increasing amplitude.


Vertebrae
T10
T11
T12
L1
L2
L3
L4
L5
Spinal cord L1 to S1
#1: 79.86 mm
#2: 57.98 mm
#3: 41.66 mm
Inferior tip of spinal cord
n = 15 individuals
Spinal cord diameter
Dorsal root entry zone
6 5 4 3 2 1 0 1 2 3 4 5 6 mm
Spinal cord length (mm)
0
–100
Measured on models elaborated from MRI scans (n = 15 individuals)
Measured on human cadavers (n = 12)
Average length of spinal segments (mm)
25
0
T12 L1 L2 L3 L4 L5 S1 S2


CT scan
Vertebrae
Intervertebral disc
MRI
Gray matter
Rootlets
White matter
Cerebrospinal fluid
Epidural fat
Roots
White matter
Gray matter
Voxel model
Rootlets


Electrode
Electric potential (a.u.)
1
0
Gray matter
White matter
Unmyelinated C-fiber
A
A
A
Myelin
A
A
Motor axon
Rootlets
Recruited structures (%)
100
0
Ipsilateral motor axon
Contralateral motor axon
Contra-lateral A
Ipsi- and contra-lateral A , C
2 3 4 5 6 7 8 9 10
Stimulation amplitude (a.u.)

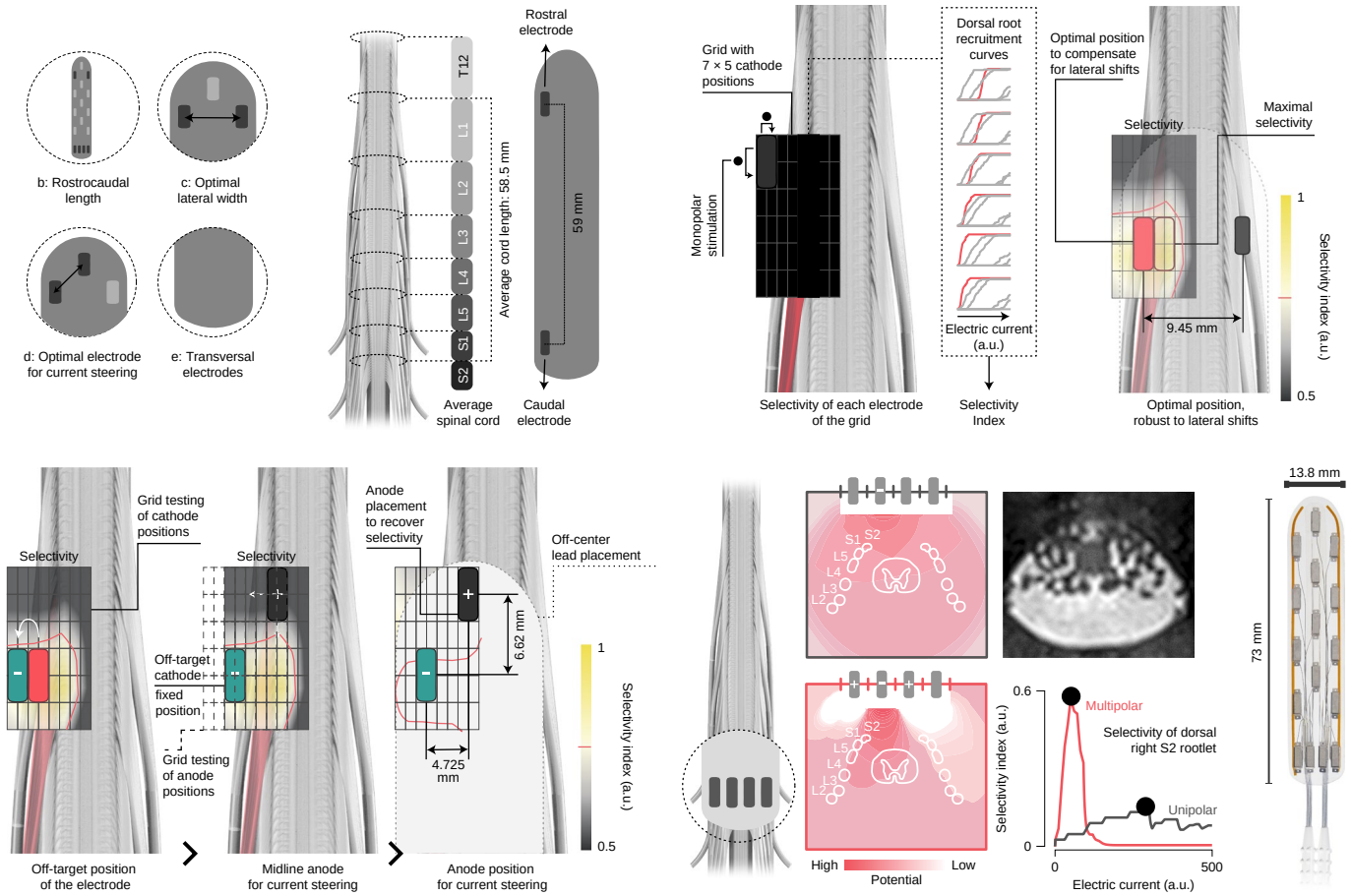


Fig. 2 | Optimal arrangement of electrodes. a, Highlight of the four features that guided the positioning of the electrodes on the new paddle lead. These features were studied using computational experiments detailed in **b**–**e**. **b**, Generalized model reconstructed from averaging all spinal cords of the atlas. The length of the new paddle lead was calculated from this model. **c**, A grid of 7 5 electrodes was positioned over each targeted rootlet bundle (here shown for the L1 dorsal root). Simulations computed a selectivity index for each electrode of the grid to determine the distributions of the lateral electrodes (red rectangle). **d**, Because of the inherent variability of dorsal root distributions and putative deviations during surgical placement, the selectivity of the cathodes may require adjustments (e.g., simulated offset as blue rectangle). Simulations determined that lateral shifts of the cathodes compensate for deviations in the medial direction, whereas anodes located over the midline steer current with bipolar stimulation. **e**, Distribution of electrical potentials when delivering unipolar versus multipolar stimulation over the dorsal roots agglutinated within the thecal sac. The transverse arrangement of electrodes enables steering the current toward the targeted sacral dorsal roots. **f**, Arrangement of electrodes on the new paddle lead.

from the mismatch between a fixed arrangement of electrodes and the large variability of spinal cord topology. We concluded that a preoperative planning was essential to optimize the positioning of the lead.

We first generated a personalized model of the spine for each participant (Fig. 3a,b). Because EES modulates motor neurons through the recruitment of large-diameter afferents, we presumed that localizing the predominant projectome of these afferents would improve the models and thus the accuracy of simulations.

To expose this projectome, we monitored the blood oxygenation level-dependent response in the spinal cord[32] when activating proprioceptors, which are innervated by large-diameter afferents. We used two methods (Extended Data Fig. 3). First, we mobilized each joint passively to elicit a proprioceptive message from the lengthened muscles. Second, we implemented a more precise method based on the application of a mechanical vibration to the tendon[33,34]. Muscle tendon vibration recruits muscle spindle afferents embedded in the muscle attached to the vibrated tendon[35].

Although proprioceptive afferents project across several segments, the recruitment of these afferents leads to the predominant activation of homonymous motor neurons[36]. Accordingly, the recruitment of proprioceptive afferents from muscles distributed at the ankle, knee and hip levels induced blood oxygenation level-dependent responses that remained confined within one or two segments (Extended Data Fig. 3). These responses exposed the predominant projectome of large-diameter afferents innervating the mobilized muscle. We integrated the projectome from key leg muscles into the personalized computational models (Extended Data Fig. 4).

To determine the optimal rostrocaudal position of the paddle lead, we implemented an algorithm that calculated the relative activation of the targeted muscles with respect to the nontargeted muscles[8] (Extended Data Fig. 4 and Supplementary Video 1).

Intraoperative validation of model predictions. We next aimed to validate the predictions of the simulations, and the relevance of improving the precision of the models with personalized features to generate these predictions. We conducted intraoperative experiments in three participants of the ongoing clinical trial STIMO (Stimulation Movement Overground; Supplementary Data Table 1 and Supplementary Video 1).

We first performed an intraoperative tridimensional CT scan to map the predicted position of the lead to the anatomy of each participant and thus guide its insertion. Once the lead was advanced to the predicted position, we quantified the selectivity of the electrodes located at each corner of the lead. We delivered single pulses of EES to elicit muscle responses that we monitored with electromyographic recordings. We quantified the selectivity of each electrode using the same algorithm as in simulations.

We then studied whether alternative locations would permit superior selectivity. Moving the lead by approximately 2 mm in the rostral or caudal direction resulted in lower selectivity, indicating that the predicted position achieved the highest performance (Fig. 3b).

We finally asked whether the personalized features of the models were important for predicting the optimal position of the lead[37]. Simulations based on a generic computational model or theoretical myotome distributions failed to reach the same accuracy as personalized models (Extended Data Fig. 5).

Superior selectivity of the new electrode arrangement. We then aimed to demonstrate that the new arrangement of electrodes enhanced the coverage and selectivity of EES compared to leads originally designed for pain treatment. We selected the Specify 5-6-5, because this lead has been the most commonly used to restore walking in humans with SCI[7–10].

To enable a direct comparison, we performed an intraoperative assessment of the Specify 5-6-5 in the same participants. The length of the Specify 5-6-5 is shorter than the new lead by 18.8 mm. Accordingly, simulations predicted that the Specify 5-6-5 would not be able to target all the dorsal roots in these participants. Intraoperative electrophysiological quantifications confirmed these predictions (Fig. 3c and Extended Data Fig. 4).

Finally, we asked whether the transverse arrangement of electrodes at the bottom of the lead enabled a more selective recruitment of dorsal roots agglutinated in the thecal sac. We found that multipolar combinations of these electrodes enhanced the selective recruitment of triceps muscles, whose motor neurons are located in sacral segments (Fig. 3d).

Neurostimulation platform. Biomimetic EES requires the delivery of concurrent stimulation waveforms that are turned on and off with a precise timing[4,8,12,21]. Moreover, many activities necessitate adjustment of stimulation parameters in closed-loop via wireless links. To support these features, we upgraded the Activa RC implantable pulse generator (IPG) with wireless communication modules (Supplementary Fig. 1). This neurostimulation platform supported real-time updates of EES frequency, amplitude and timing from up to 10 stimulation waveforms[8]. The new paddle lead was interfaced with the Activa RC, which was implanted in the abdomen.

We also developed a new software operating through touchscreen interfaces to enable the rapid configuration of activity-dependent stimulation programs (Fig. 4c). To simplify these configurations, wireless recordings of kinematics and muscle activity are displayed in real time, concomitantly to EES waveforms (Supplementary Fig. 1 and Supplementary Video 2).

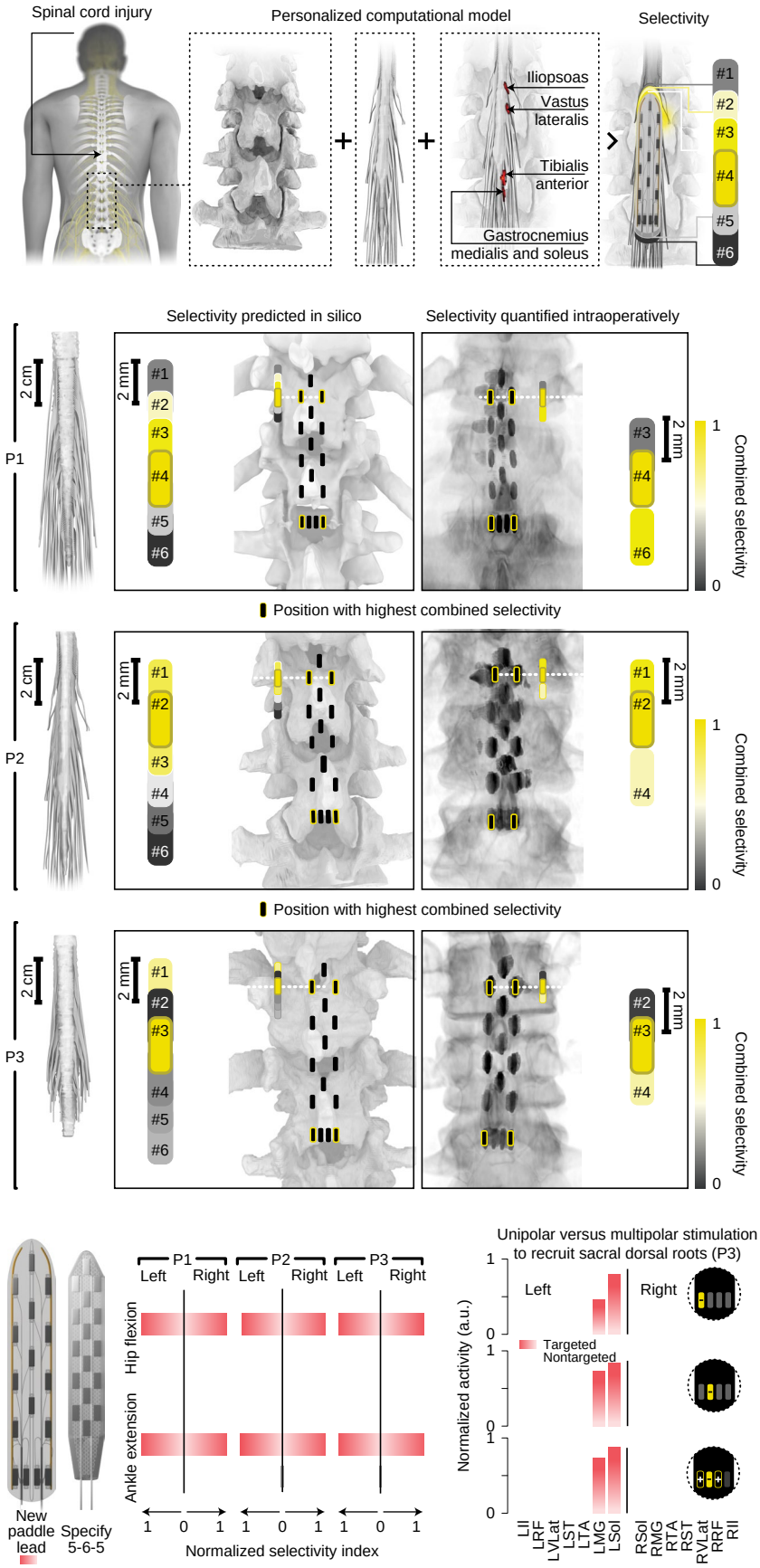
Immediate recovery of walking after complete paralysis. Our next objective was to demonstrate the superior performance of the new lead to restore walking after SCI. Previous studies showed that a subset of individuals with complete motor paralysis could step with EES following many months of training[7,10]. Here, we aimed to restore independent stepping on the first day of stimulation in all the participants.

We first assembled preoperative and intraoperative information into a library of cathode and anode configurations targeting the individual dorsal roots (Extended Data Fig. 6). Each configuration aimed to modulate a specific ensemble of motor neurons that are confined within circumscribed regions of the spinal cord, termed motor hotspots (Fig. 4b). Each configuration was then optimized based on the responses elicited by EES. For this purpose, brief trains (500 ms) of stimulation were delivered in a supine position, because bursts elicited ample leg movements that identified potential undesired movements and thus facilitated the fine-tuning of anode–cathode combinations (Extended Data Fig. 6 and Supplementary Video 2). Pulse frequencies were adjusted for extensor (20 Hz) versus flexor (100 Hz) muscles, as the motor neurons innervating these muscles exhibit distinct preferential activation frequencies[8] (Extended Data Fig. 7). Elaborating this library did not last longer than 1 hour.

Once the library was configured, the temporal sequence of EES pulses was optimized for each participant. Walking involves stereotypical spatiotemporal patterns of motor hotspot activation that reflect changes in body mechanics[24,25] (Fig. 4a,b). Therefore, the next step consisted of injecting the electrode configurations targeting each motor hotspot into pre-established sequences of EES pulses that reproduce the natural pattern of motor hotspot activation during walking[4,8,21,23] (Fig. 4b). Finally, EES parameters were fine-tuned through a stimulation scheduler displayed on the software. This fine-tuning involved interactions with the physical therapist and participant who was attempting to walk (Fig. 4c). This procedure allowed the configuration of EES programs for walking within 1 hour.

All three participants exhibited complete sensorimotor paralysis (Supplementary Table 1). They were unable to take any step, and muscles remained quiescent during these attempts (Extended Data Fig. 8). On the first day, all three participants could step independently on a treadmill, although gait patterns exhibited poor extension components. Consequently, substantial amounts of body-weight support were necessary (Fig. 4d). After 1–3 additional days, gait patterns were sufficiently optimized to enable the three participants to ambulate independently overground while supported in a multidirectional body-weight support system[38] (Fig. 4d and Supplementary Video 2). This recovery involved the production of substantial activity in leg muscles that coincided with

Fig. 3 | Preoperative planning and intraoperative validation. a, CT scan combined with structural and functional MRI acquisitions enabled the personalization of computational models predicting the interactions between the location of EES and the recruitment of afferents in the dorsal roots. **b**, For each participant, simulations (left) calculated the relative selectivity of the paddle lead for six positions separated by 2 mm, as shown in the vertical bars positioned over the computational model and their enlarged version next to each bar. The selectivity of electrodes located at each corner of the paddle lead is aggregated in a combined (color-coded) selectivity index. The same procedure was conducted intraoperatively (right) for three positions of the paddle lead, including the optimal position predicted by the model. Representations are the same as in the computational simulations. The final surgical positioning of the paddle lead is displayed in the reconstructed CT images. **c**, Bar plots reporting the selectivity of electrodes from the new paddle lead (red) and Specify 5-6-5 (gray) to recruit muscles eliciting hip flexion and ankle extension. P, participant. **d**, Bar plots reporting the amplitude of muscle responses when stimulating with monopolar versus multipolar electrode configurations showing the ability of the transverse electrode arrangement to selectively recruit sacral roots despite the agglutination of all lumbar dorsal roots within the stimulated region. LII, left iliopsoas; LMG, left medial gastrocnemius; LRF, left rectus femoris; LSol, left soleus; LVLat, left vastus lateralis; LST, left semitendinosus; LTA, left tibialis anterior; RII, right iliopsoas; RMG, right medial gastrocnemius; RRF, right rectus femoris; RSol, right soleus; RST, right semitendinosus; RTA, right tibialis anterior; RVLat, right vastus lateralis.


Spinal cord injury
Personalized computational model
Selectivity
Iliopsoas
Vastus lateralis
Tibialis anterior
Gastrocnemius medialis and soleus
#1
#2
#3
#4
#5
#6
Selectivity predicted in silico
Selectivity quantified intraoperatively
P1
P2
P3
2 cm
2 mm
Combined selectivity
1
0
Position with highest combined selectivity
New paddle lead
Specify 5-6-5
Left
Right
Hip flexion
Ankle extension
Normalized selectivity index
Unipolar versus multipolar stimulation to recruit sacral dorsal roots (P3)
Normalized activity (a.u.)
Targeted
Nontargeted
LIl
LRF
LVLat
LST
LTA
LMG
LSol
RSol
RMG
RTA
RST
RVLat
RRF
RIl

pronounced excursions of hip, knee and ankle joints (Fig. 4b and Extended Data Fig. 8).

Two out of the three participants could modulate the amplitude of leg movements when asked to increase their step length voluntarily (Extended Data Fig. 8). Contrary to the fatigue that rapidly occurs with direct neuromuscular stimulation[39], the participants could produce up to 300 independent steps as early as the first day of stimulation (Extended Data Fig. 8).

Extension to other motor activities. We reasoned that the principles through which EES restores walking could support the configuration of EES programs to enable other motor activities.

To test this possibility, we configured activity-specific stimulation programs that enabled the three participants to use their legs to swim in the water or pedal actively on a motorized bike (Fig. 4e and Supplementary Video 3). EES programs also supported rehabilitation exercises such as squats or leg press (Fig. 4e and Supplementary Video 3).

We applied the same principles to target trunk muscles (Extended Data Fig. 9). Indeed, the participants showed impairments in the control of trunk postures (Extended Data Fig. 10). EES programs targeting trunk muscles normalized trunk postures (Fig. 5) and improved the control of trunk movements. For example, participants who exhibited difficulties to regain an upright trunk posture from a flexed position performed this task with ease, as captured in the marked increase in the speed of these executions (Fig. 5e and Supplementary Video 3).

Recovery of independence in ecological settings. Activity-dependent stimulation programs enabled the immediate recovery of trunk and leg motor functions in people with complete paralysis. Although weight-bearing capacities and overall performances remained limited at this stage, this recovery provided the opportunity to engage the neuromuscular system into sustained and active training sessions. We thus asked whether performance would improve with practice and whether these improvements would be sufficient to regain some independence in ecological settings.

The three participants underwent a 5-month neurorehabilitation program during which EES enabled them to stand, walk and perform a broad range of exercises four or five times per week. We developed a simplified software interface that allowed participants and physical therapists to switch between activity-dependent stimulation programs and fine-tune key parameters of these programs. We also equipped the assistive devices with ergonomic clickers that trigger EES programs upon desire. For example, they could switch between standing and walking or between the swing and stance phases of gait (Supplementary Fig. 1). Participants could select EES sequences that were executed in open-loop or triggered with clickers or closed-loop control of these sequences based on wearable sensors (Supplementary Fig. 1).

Performance improved dramatically. All three participants progressively regained full weight-bearing capacities (Fig. 6b), which translated into the ability to stand independently in community settings (Fig. 6d and Supplementary Video 4). Improvement of gait patterns and weight-bearing capacities allowed them to walk independently with the help of a front-wheel walker for stability, which enabled the performance of the 10-m and 6-min walk test without any assistance (Fig. 6c and Supplementary Video 2). One of the participants even regained the ability to climb a staircase and progress over complex terrain (Supplementary Video 4). Participants could also ride a recumbent trike powered with the arms and legs (Fig. 6). Finally, improved control of trunk postures allowed the practice of leisure activities such as boxing, enjoying a drink while standing at a bar or paddling a canoe on a lake (Fig. 6 and Supplementary Video 4).

These improvements coincided with a substantial increase in the mass of leg and trunk muscles (Fig. 6f). Moreover, two of the participants recovered the ability to activate proximal muscles voluntarily without EES (Supplementary Fig. 2).

Discussion

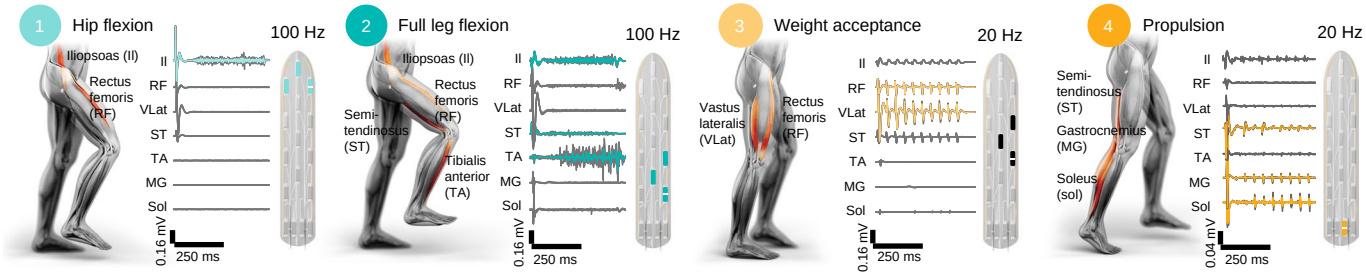
Here, we show that biomimetic EES enabled the recovery of standing, walking, cycling, swimming and trunk control within 1 day in three individuals with chronic complete paralysis. After neurorehabilitation, the three treated individuals were able to leverage biomimetic EES to perform these activities in the community. Central to this radically increased efficacy compared to previous studies[7,10] was an arrangement of electrodes that targeted the ensemble of sacral, lumbar and low-thoracic dorsal roots involved in the production of leg and trunk movements, combined with a software that renders the configuration of activity-dependent stimulation programs rapid, simple and predictable.

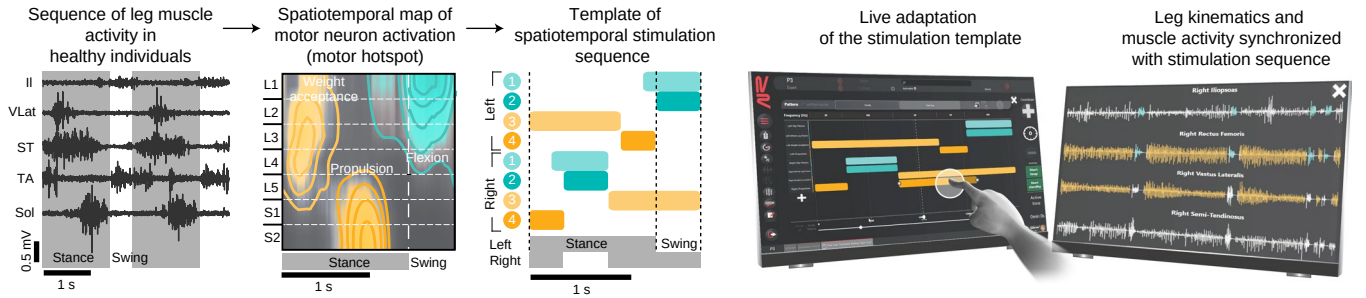
Although the three participants could ambulate independently, it is important to point out that they did not regain natural movements. Yet, this recovery was sufficient to perform various activities for extensive periods of time. Moreover, two participants were able to modulate leg movements during EES, suggesting that the stimulation boosted signals from residual descending pathways. The recovery of volitional muscle activation without EES following neurorehabilitation reinforced this interpretation. We previously showed that the remodeling of residual descending pathways mediated this recovery[5,6]. We thus surmised that a small number of nerve fibers had survived the injury but that these fibers had remained functionally silent due to the hypoactivity below the injury[40].

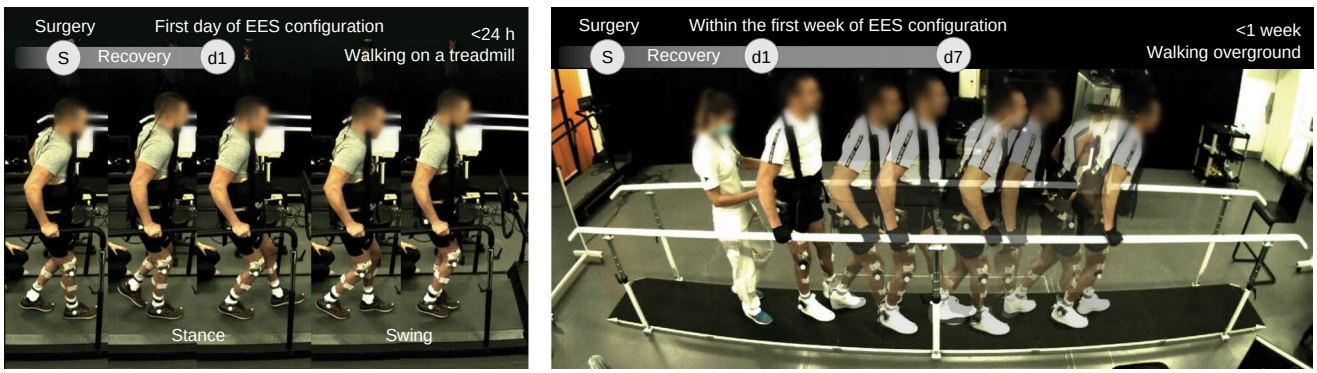
We previously showed that neurorehabilitation supported by EES mediated a more extensive neurological recovery after incomplete SCI[4], emphasizing the logical importance of residual pathways to promote recovery. Therefore, the development of biological repair interventions remains critical to enhance recovery with neurorehabilitation supported by EES[41,42]. Biomimetic EES may also enable active and sustained movements in the early phase after SCI, allowing to take full advantage of natural repair mechanisms to augment neurological recovery.

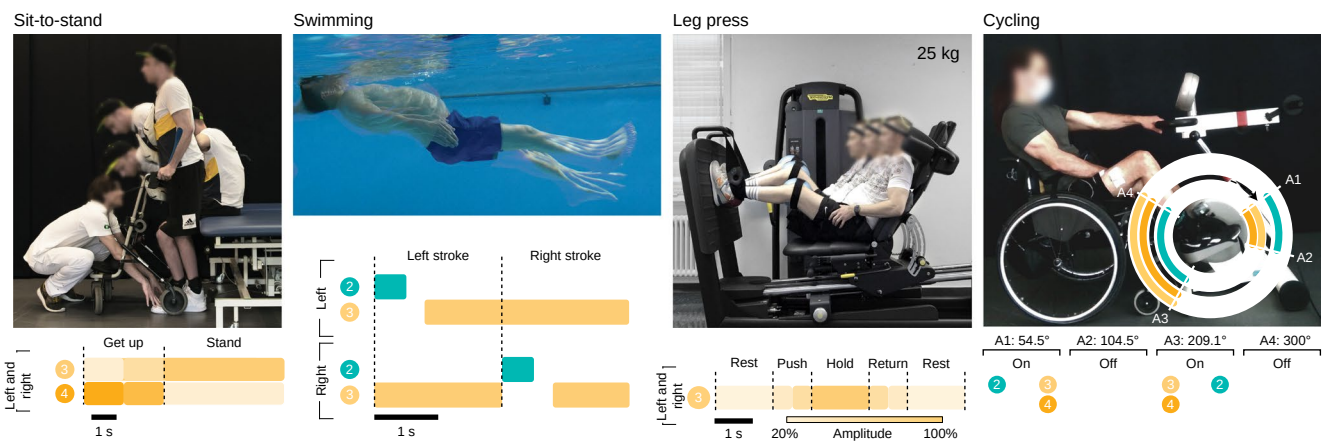
The development of the paddle lead required a number of tradeoffs to circumvent the variable topology of the dorsal roots across the human population. Although this new lead allowed the validation of our therapeutic concepts, the fixed coverage and uniform distribution of electrodes were inevitably suboptimal. Therefore, we anticipate that delivering this therapy across the human population may require a library of paddle leads or even personalized leads.

Fig. 4 | Configuration of activity-dependent stimulation programs. a, Library of optimized anode and cathode configurations and stimulation frequencies to modulate motor pools associated with the key phases of gait, as highlighted with the color code. **b**, Sequence of muscle activity underlying walking in healthy people, converted into a spatiotemporal map of motor neuron activity that highlights the timing and location of motor hotspot activation; translated into a preprogrammed sequence of stimulation bursts (template) that aims to reproduce this activation pattern. Color code as in **a**. The configurations of electrodes targeting each hotspot are derived from the library and injected into this template. **c**, Software enabling live adjustments of stimulation patterns and parameters based on real-time feedback from muscle activity and kinematic sensors that are synchronized with stimulation sequences. **d**, Walking on a treadmill with stimulation after less than 1 hour of configuration and independent walking between parallel bars less than 1 week after the onset of the therapy, including sequence of stimulation and underlying muscle activity. d, day. **e**, Chronophotography of sit-to-stand, swimming, leg-press and motomed exercises enabled by activity-specific stimulation programs (displayed at the bottom of each chronophotograph).


1
Hip flexion
100 Hz
Iliopsoas (Il)
Rectus femoris (RF)
Il
RF
VLat
ST
TA
MG
Sol
0.16 mV
250 ms
2
Full leg flexion
100 Hz
Iliopsoas (Il)
Rectus femoris (RF)
Semi-tendinosus (ST)
Tibialis anterior (TA)
0.16 mV
250 ms
3
Weight acceptance
20 Hz
Vastus lateralis (VLat)
Rectus femoris (RF)
0.16 mV
250 ms
4
Propulsion
20 Hz
Semi-tendinosus (ST)
Gastrocnemius (MG)
Soleus (sol)
0.04 mV
250 ms


Sequence of leg muscle activity in healthy individuals
Spatiotemporal map of motor neuron activation (motor hotspot)
Template of spatiotemporal stimulation sequence
Live adaptation of the stimulation template
Leg kinematics and muscle activity synchronized with stimulation sequence
Il
VLat
ST
TA
Sol
0.5 mV
Stance
Swing
1 s
L1
L2
L3
L4
L5
S1
S2
Weight acceptance
Propulsion
Flexion
Left
Right
Right Iliopsoas
Right Rectus Femoris
Right Vastus Lateralis
Right Semi-Tendinosus


Surgery
First day of EES configuration
S
Recovery
d1
<24 h
Walking on a treadmill
Stance
Swing
Surgery
Within the first week of EES configuration
S
Recovery
d1
d7
<1 week
Walking overground
Left
Right
Stance
Swing
1 s
Il
VLat
ST
TA
Sol
0.1 mV
0.04 mV


Sit-to-stand
Get up
Stand
Left and right
1 s
Swimming
Left stroke
Right stroke
Left
Right
1 s
Leg press
25 kg
Rest
Push
Hold
Return
Rest
Left and right
1 s
20%
Amplitude
100%
Cycling
A1
A2
A3
A4
A1: 54.5°
On
A2: 104.5°
Off
A3: 209.1°
On
A4: 300°
Off

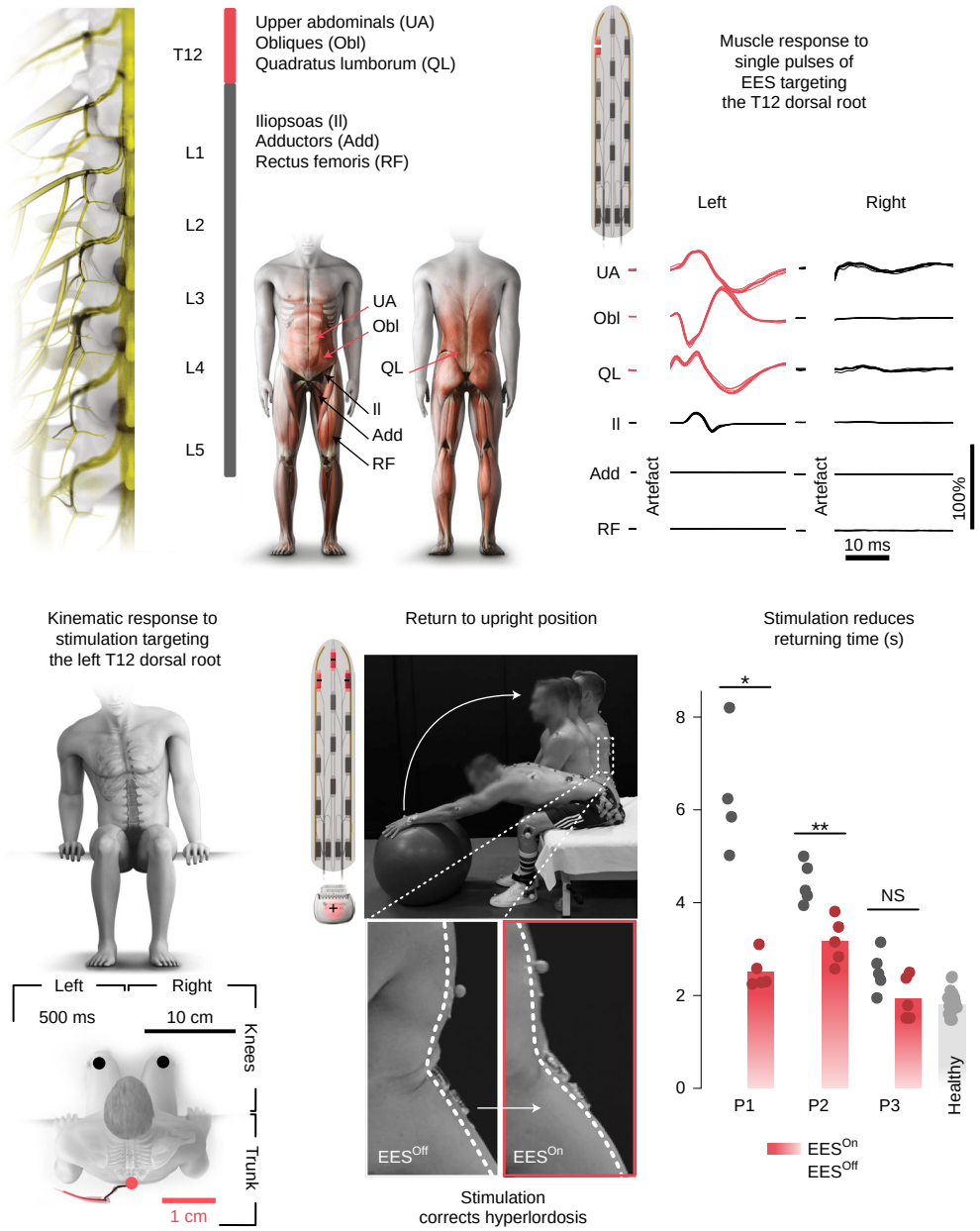


Fig. 5 | Configuration of trunk-specific stimulation programs. a,**b**, Stimulation of the dorsal root projections to the T12 spinal segment modulates trunk and abdominal muscles (**a**), as shown in muscle responses (**b**). **c**, Temporal course (color-coded) of coronal plane trunk trajectory elicited by side-specific stimulation. **d**, Chronophotography of a sequence of trunk flexion and extension. The onsets highlight trunk posture at rest without and with a stimulation program optimized for modulation of motor pools innervating trunk muscles. **e**, Bar plots reporting the time necessary to complete the return phase (extension) of the flexion/extension sequence of trunk movements for the three participants compared to five healthy individuals (Mann–Whitney test, two tailed: P1, P 0.0159; P2, P 0.0079; P3: P 1429; *P 0.05; **P 0.01). Dots represent the number of repeated movements for each patient (N 5 repetitions per patient and per stimulation condition).

Although current regulations for silicone-based medical devices are not compatible with this possibility, microfabrication processes may provide a realistic path for personalized leads[43,44]. In turn, our computational framework enables selecting the optimal paddle lead for each patient and planning its surgical positioning for optimal selectivity. With a large choice of leads or increased number of electrodes, the preoperative planning may also be simplified because the identification of projectomes with functional MRI (fMRI) acquisitions would not be necessary. High-density electrode arrays are under development, but the challenge may reside in the availability of pulse generators to control the stimulation. Indeed, biomimetic EES requires neurostimulation platforms designed for closed-loop operations, combining ultrafast and reliable wireless communication with control units that can decode motor intentions from wearable or implanted sensors, including interfaces measuring brain activity[21,45,46].

We only targeted the dorsal roots projecting to the low thoracic segment. However, the selective modulation of trunk muscles suggested that targeting additional thoracic dorsal roots will further improve the recovery of trunk movements[29,47].

These therapeutic concepts are relevant to address other neurological functions that are prioritized by people with SCI[48]. Indeed, EES can regulate bladder and bowel functions[49], hemodynamics[50,51]

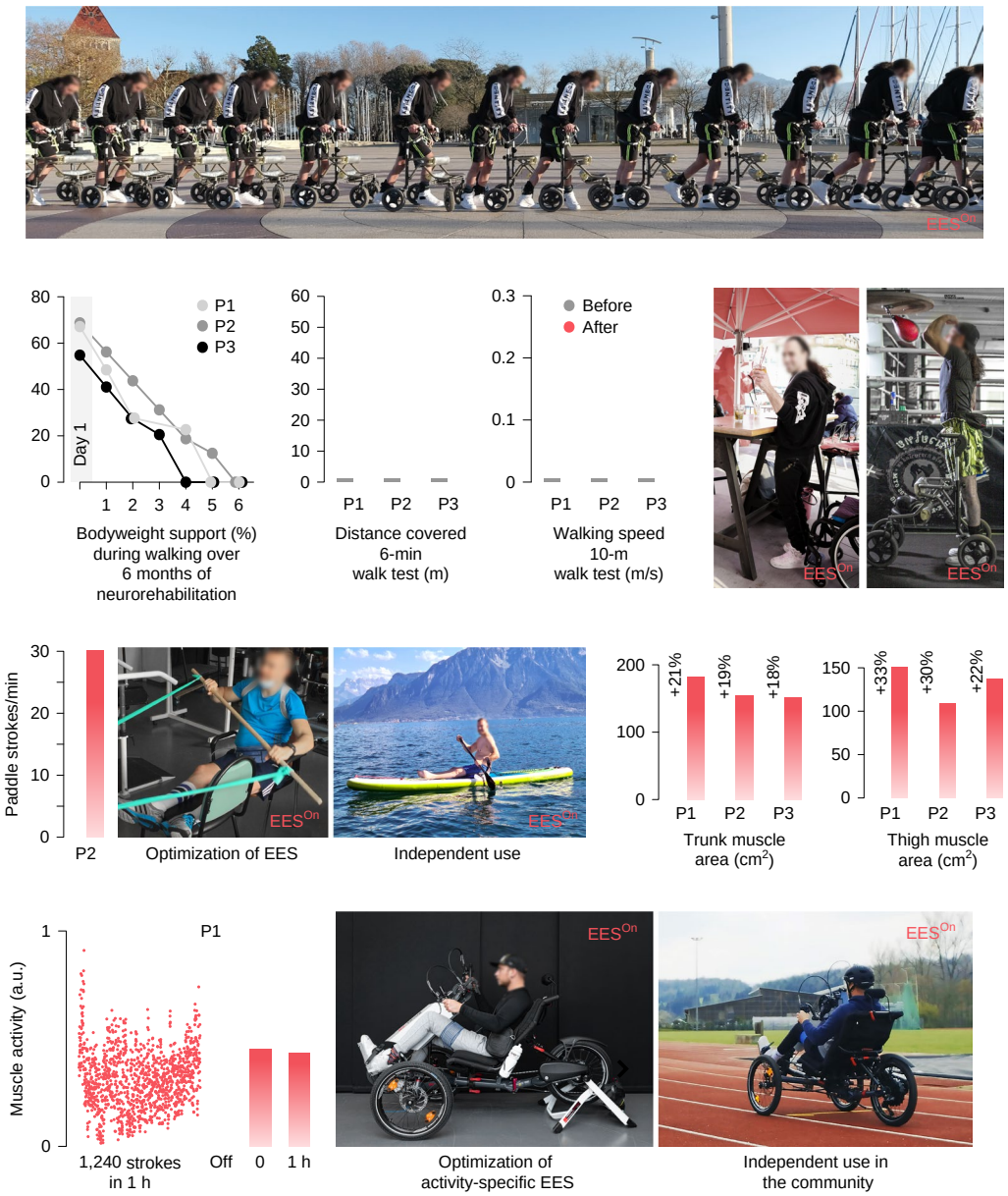


Fig. 6 | Recovery of independence in the community. a, Chronophotography of independent walking outdoors after 6 months of practice with activity-specific programs. **b**, Optimal body weight support to enable walking during neurorehabilitation. **c**, Bar plots reporting performance in the 6-min walk test and 10-m walk test before and after neurorehabilitation with activity-specific stimulation programs. No assistance was provided during these tests. **d**, Standing for extensive periods of time for boxing or enjoying a drink at a high table of a bar. See also **Supplementary Video 4. e**, Stimulation programs for trunk stability while paddling were developed in the lab, and then used to support paddling activity on a lake. Bar plots report the number of paddle strokes per minute with and without EES. **f**, Bar plots reporting changes in thigh and trunk muscle mass, quantified as total/specific cross-sectional area. **g**, Amplitude of muscle activity for each of N 1,240 strokes performed over 1 hour. Bar plots report the mean amplitude of muscle activity without EES (N 27 cycles, gray) and calculated during the N 100 first and N 100 last cycles (red). Photographs illustrate the setting for the development of cycling stimulation and its use in community settings.

and arm/hand movements[30]. The regions involved in the regulation of these functions are distributed along the neuraxis, suggesting that purpose-made neurotechnologies targeting the dorsal roots projecting to these specific regions are necessary to develop effective treatments. Targeting some of these functions may require highly specific stimulation of certain dorsal roots, which could be achieved with the direct neuromodulation of dorsal root ganglia[52].

Scaling up these therapies across clinical centers worldwide will require artificial intelligence assistants to support neurosurgical interventions and EES program configurations. Advances in machine-learning algorithms and cloud-based computing for medical applications established the technological landscape to realize this transition.

Biomimetic EES restored trunk and leg motor functions within 1 day after complete sensorimotor paralysis and mediated the recovery of some independence in ecological settings after neurorehabilitation. This recovery, combined with our previous findings in people with incomplete SCI[8], is opening a realistic pathway to deploy a therapy that will mediate clinically meaningful improvements in people presenting with a broad range of SCI severities.

Online content

Any methods, additional references, Nature Research reporting summaries, source data, extended data, supplementary information, acknowledgements, peer review information; details of author contributions and competing interests; and statements of data and code availability are available at https://doi.org/10.1038/s41591-021-01663-5.

Received: 25 May 2021; Accepted: 16 December 2021;
Published online: 07 February 2022

References

1. Ichiyama, R. M. et al. Step training reinforces specific spinal locomotor circuitry in adult spinal rats. J. Neurosci. 28, 7370–7375 (2008).
2. Courtine, G. et al. Transformation of nonfunctional spinal circuits into functional states after the loss of brain input. Nat. Neurosci. 12, 1333–1342 (2009).
3. Wenger, N. et al. Closed-loop neuromodulation of spinal sensorimotor circuits controls refined locomotion after complete spinal cord injury. Sci. Transl. Med. 6, 255ra133–255ra133 (2014).
4. Wenger, N. et al. Spatiotemporal neuromodulation therapies engaging muscle synergies improve motor control after spinal cord injury. Nat. Med. 22, 138–145 (2016).
5. Brand, Rvanden et al. Restoring voluntary control of locomotion after paralyzing spinal cord injury. Science 336, 1182–1185 (2012).
6. Asboth, L. et al. Cortico–reticulo–spinal circuit reorganization enables functional recovery after severe spinal cord contusion. Nat. Neurosci. 21, 576–588 (2018).
7. Gill, M. L. et al. Neuromodulation of lumbosacral spinal networks enables independent stepping after complete paraplegia. Nat. Med. 24, 1677–1682 (2018).
8. Wagner, F. B. et al. Targeted neurotechnology restores walking in humans with spinal cord injury. Nature 563, 65–71 (2018).
9. Harkema, S. et al. Effect of epidural stimulation of the lumbosacral spinal cord on voluntary movement, standing, and assisted stepping after motor complete paraplegia: a case study. Lancet 377, 1938–1947 (2011).
10. Angeli, C. A. et al. Recovery of over-ground walking after chronic motor complete spinal cord injury. N. Engl. J. Med. 379, 1244–1250 (2018).
11. Danner, S. M. et al. Human spinal locomotor control is based on flexibly organized burst generators. Brain 138, 577–588 (2015).
12. Formento, E. et al. Electrical spinal cord stimulation must preserve proprioception to enable locomotion in humans with spinal cord injury. Nat. Neurosci. 21, 1728–1741 (2018).
13. Herman, R., He, J., D'Luzansky, S., Willis, W. & Dilli, S. Spinal cord stimulation facilitates functional walking in a chronic, incomplete spinal cord injured. Spinal Cord. 40, 65–68 (2002).
14. Barolat, G., Myklebust, J. B. & Wenninger, W. Enhancement of voluntary motor function following spinal cord stimulation: case study. Appl. Neurophysiol. 49, 307–314 (1986).
15. Dimitrijevic, M. R., Gerasimenko, Y. & Pinter, M. M. Evidence for a spinal central pattern generator in humans. Ann. N Y Acad. Sci. 860, 360–376 (1998).
16. & Darrow, D. et al. Epidural spinal cord stimulation facilitates immediate restoration of dormant motor and autonomic supraspinal pathways after chronic neurologically complete spinal cord injury. J. Neurotrauma. 36, 2325–2336 (2019).
17. Gerasimenko, Y. P. et al. Spinal cord reflexes induced by epidural spinal cord stimulation in normal awake rats. J. Neurosci. Methods 157, 253–263 (2006).
18. Rattay, F. et al. Mechanisms of electrical stimulation with neural prostheses. Neuromodulation 6, 42–56 (2003).
19. Capogrosso, M. et al. A computational model for epidural electrical stimulation of spinal sensorimotor circuits. J. Neurosci. 33, 19326–19340 (2013).
20. Moraud, E. M. et al. Mechanisms underlying the neuromodulation of spinal circuits for correcting gait and balance deficits after spinal cord injury. Neuron 89, 814–828 (2016).
21. Capogrosso, M. et al. A brain–spine interface alleviating gait deficits after spinal cord injury in primates. Nature 539, 284–288 (2016).
22. Minev, I. R. et al. Electronic dura mater for long-term multimodal neural interfaces. Science 347, 159–163 (2015).
23. Capogrosso, M. et al. Configuration of electrical spinal cord stimulation through real-time processing of gait kinematics. Nat. Protoc. 13, 2031–2061 (2018).
24. Yakovenko, S., Mushahwar, V., VanderHorst, V., Holstege, G. & Prochazka, A. Spatiotemporal activation of lumbosacral motoneurons in the locomotor step cycle. J. Neurophysiol. 87, 1542–1553 (2002).
25. Cappellini, G., Ivanenko, Y. P., Dominici, N., Poppele, R. E. & Lacquaniti, F. Migration of motor pool activity in the spinal cord reflects body mechanics in human locomotion. J. Neurophysiol. 104, 3064–3073 (2010).
26. Molnar, G. & Barolat, G. Principles of cord activation during spinal cord stimulation. Neuromodulation 17, 12–21 (2014).
27. Minassian, K., Hofstoetter, U., Tansey, K. & Mayr, W. Neuromodulation of lower limb motor control in restorative neurology. Clin. Neurol. Neurosurg. 114, 489–497 (2012).
28. Moraud, E. M. et al. Closed-loop control of trunk posture improves locomotion through the regulation of leg proprioceptive feedback after spinal cord injury. Sci. Rep. 8, 76 (2018).
29. Gill, M. et al. Epidural electrical stimulation of the lumbosacral spinal cord improves trunk stability during seated reaching in two humans with severe thoracic spinal cord injury. Front. Syst. Neurosci. 14, 79 (2020).
30. Greiner, N. et al. Recruitment of upper-limb motoneurons with epidural electrical stimulation of the cervical spinal cord. Nat. Commun. 12, 435 (2021).
31. Neufeld, E., Szczerba, D., Chavannes, N. & Kuster, N. A novel medical image data-based multi-physics simulation platform for computational life sciences. Interface Focus. 3, 20120058 (2013).
32. Kinany, N., Pirondini, E., Micera, S. & Ville, D. V. D. Dynamic functional connectivity of resting-state spinal cord fMRI reveals fine-grained intrinsic architecture. Neuron 108, 424–435 (2020).
33. Landelle, C. et al. Functional brain changes in the elderly for the perception of hand movements: a greater impairment occurs in proprioception than touch. Neuroimage 220, 117056 (2020).
34. Courtine, G., Nunzio, A. M. D., Schmid, M., Beretta, M. V. & Schieppati, M. Stance- and locomotion-dependent processing of vibration-induced proprioceptive inflow from multiple muscles in humans. J. Neurophysiol. 97, 772–779 (2007).
35. Roll, J. P., Vedel, J. P. & Ribot, E. Alteration of proprioceptive messages induced by tendon vibration in man: a microneurographic study. Exp. Brain Res. 76, 213–222 (1989).
36. Pierrot-Deseilligny, E. & Burke, D. e Circuitry of the Human Spinal Cord (Cambridge University Press, 2005).
37. Lempka, S. F. et al. Patient specific analysis of neural activation during spinal cord stimulation for pain. Neuromodulation 23, 572–581 (2020).
38. Mignardot, J.-B. et al. A multidirectional gravity-assist algorithm that enhances locomotor control in patients with stroke or spinal cord injury. Sci. Transl. Med. 9, eaah3621 (2017).
39. Shokur, S., Mazzoni, A., Schiavone, G., Weber, D. J. & Micera, S. A modular strategy for next-generation upper-limb sensory-motor neuroprostheses. Med 2, 912–937 (2021).
40. Edgerton, V. R. & Harkema, S. Epidural stimulation of the spinal cord in spinal cord injury: current status and future challenges. Expert Rev. Neurother. 11, 1351–1353 (2011).
41. Courtine, G. & Sofroniew, M. V. Spinal cord repair: advances in biology and technology. Nat. Med. 25, 898–908 (2019).
42. Morse, L. R. et al. Meeting proceedings for SCI 2020: launching a decade of disruption in spinal cord injury research. J. Neurotrauma. 38, 1251–1266 (2021).
43. Schiavone, G. et al. Soft, implantable bioelectronic interfaces for translational research. Adv. Mater. 32, 1906512 (2020).
44. Barra, B. et al. Epidural electrical stimulation of the cervical dorsal roots restores voluntary arm control in paralyzed monkeys. Preprint at bioRxiv https://doi.org/10.1101/2020.11.13.379750 (2021).
45. Bonizzato, M. et al. Brain-controlled modulation of spinal circuits improves recovery from spinal cord injury. Nat. Commun. 9, 3015 (2018).
46. Benabid, A. L. et al. An exoskeleton controlled by an epidural wireless brain–machine interface in a tetraplegic patient: a proof-of-concept demonstration. Lancet Neurol. 18, 1112–1122 (2019).
47. Chen, C.-L. et al. The relationship between sitting stability and functional performance in patients with paraplegia. Arch. Phys. Med. Rehab. 84, 1276–1281 (2003).
48. Anderson, K. D. Targeting recovery: priorities of the spinal cord-injured population. J. Neurotrauma. 21, 1371–1383 (2004).
49. Herrity, A. N., Williams, C. S., Angeli, C. A., Harkema, S. J. & Hubscher, C. H. Lumbosacral spinal cord epidural stimulation improves voiding function after human spinal cord injury. Sci. Rep. 8, 8688 (2018).
50. Squair, J. W. et al. Neuroprosthetic baroreflex controls haemodynamics after spinal cord injury. Nature 590, 308–314 (2021).
51. Ditterline, B. E. L. et al. Beneficial cardiac structural and functional adaptations after lumbosacral spinal cord epidural stimulation and task-specific interventions: a pilot study. Front Neurosci. 14, 554018 (2020).
52. Soloukey, S. et al. The dorsal root ganglion as a novel neuromodulatory target to evoke strong and reproducible motor responses in chronic motor complete spinal cord injury: a case series of five patients. Neuromodulation 24, 779–793 (2021).

Publisher's note Springer Nature remains neutral with regard to jurisdictional claims in published maps and institutional affiliations.

© The Author(s), under exclusive licence to Springer Nature America, Inc. 2022

[1]Center for Neuroprosthetics and Brain Mind Institute, School of Life Sciences, Swiss Federal Institute of Technology (EPFL), Lausanne, Switzerland. [2]Department of Clinical Neuroscience, Lausanne University Hospital (CHUV) and University of Lausanne (UNIL), Lausanne, Switzerland. [3]Defitech Center for Interventional Neurotherapies (NeuroRestore), EPFL/CHUV/UNIL, Lausanne, Switzerland. [4]ONWARD Medical, Lausanne, Switzerland. [5]Foundation for Research on Information Technologies in Society, Zurich, Switzerland. [6]Department for Information Technology and Electrical Engineering, Swiss Federal Institute of Technology, Zurich, Switzerland. [7]Department of Diagnostic and Interventional Radiology, CHUV/UNIL, Lausanne, Switzerland. [8]Institute of Bioengineering, EPFL, Lausanne, Switzerland. [9]The BioRobotics Institute, Scuola Superiore Sant'Anna, Pisa, Italy. [10]Department of Neurosurgery, CHUV, Lausanne, Switzerland. [11]Biomedical Imaging Center, MR Section, CHUV, Lausanne, Switzerland. [12]University Medical Center Utrecht, Utrecht, Netherlands. [13]Fondation Campus Biotech Genève, Geneva, Switzerland. [14]Institut des Neurosciences de la Timone, Aix-Marseille University, CNRS, Marseille, France. [15]ZurichMedTech, Zurich, Switzerland. [16]Medtronic, Minneapolis, MN, USA. [17]Department of Engineering Science, University of Oxford, Oxford, United Kingdom. [18]Medical Materials and Implants, Technical University of Munich, Munich, Germany. [19]Center for Medical Physics and Biomedical Engineering, Medical University of Vienna, Vienna, Austria. [20]Laboratoire de Neurosciences Cognitives, Aix-Marseille University, CNRS, Marseille, France. [21]Bertarelli Foundation, Translational Neuroengineering, Center for Neuroprosthetics and Institute of Bioengineering, School of Bioengineering, EPFL, Lausanne, Switzerland. [22]Department of Radiology and Medical Informatics, University of Geneva, Geneva, Switzerland. [23]Department of Neurosurgery, Radboud University Medical Center Nijmegen, Nijmegen, Netherlands. [24]Department of Neuroscience and Movement Science, University of Fribourg, Fribourg, Switzerland. [25]Department of Neurological Surgery, University of Pittsburgh, Pittsburgh, PA, USA. [26]Institut des Maladies Neurodégénératives (CNRS UMR 5293), Université de Bordeaux, Bordeaux, France. [27]These authors contributed equally: Andreas Rowald, Salif Komi, Robin Demesmaeker. [28]These authors jointly supervised this work: Fabien Wagner, Jocelyne Bloch, Gregoire Courtine. ✉e-mail: jocelyne.bloch@chuv.ch; gregoire.courtine@epfl.ch

Methods

Study design and objectives. All experiments were carried out as part of the ongoing clinical feasibility study STIMO, which investigates the effects of spatiotemporal EES combined with weight-supported overground locomotor training on the recovery of motor function after SCI. This study was approved by the Swiss ethical authorities (Swissethics protocol number 04/2014 project ID PB_2016-00886, Swissmedic protocol 2016-MD-0002) and was conducted in accordance with the Declaration of Helsinki. All participants signed a written informed consent before their participation. More information at www.clinicaltrials.gov (NCT02936453). All surgical and experimental procedures were performed at the Lausanne University Hospital (CHUV). The study involved assessments before surgery, the surgical implantation of the neurostimulation system, a 1-month period during which EES protocols were configured, and a 5-month rehabilitation period with physiotherapists taking place four or five times per week for 1–3 hours. The rehabilitation program was personalized based on the participants' improvements. At the end of the rehabilitation period, the participants were given the opportunity to be enrolled in a study extension phase during which they could continue using the neurostimulation system at home. They are currently followed up on a regular basis by the study team (for up to 6 years).

Study participants. Three individuals with a traumatic thoracic SCI participated in the study. Their neurological status was evaluated according to the International Standards for Neurological Classification of Spinal Cord Injury (ISNCSCI)[53] and is reported in Supplementary Data Table 1. At the time of study enrollment, the following characteristics for the participants were made. Participant P1 was 32 years old and classified with a motor and sensory complete (AIS-A) T4 lesion that had occurred 9 years earlier during a motor bike accident. He presented with bilateral leg paralysis, with motor scores of 0 on all key leg muscles. He could neither stand nor ambulate at all (Walking Index for Spinal Cord Injury score: 0), despite extensive participation in physical exercise with adapted devices for home use. Participant P2 was 41 years old and classified with a motor and sensory complete (AIS-A) T6/T7 lesion that had occurred 1 year before his enrollment during a motor bike accident. He presented with bilateral flaccid leg paralysis, with motor scores of 0 on all key leg muscles. He did not have any spasticity in his legs and could neither stand nor ambulate at all (Walking Index for Spinal Cord Injury score: 0), despite extensive participation in physical exercise with adapted devices for home use. Participant P3 was 29 years old and classified with a motor complete (AIS-B) T5/T6 lesion that had occurred 3 years earlier during a motor bike accident. He presented with bilateral spastic leg paralysis, with sensory and motor scores of 0 on all key leg muscles. He was classified as AIS-B due to the presence of deep anal pressure.

Cadaver analysis. The 12 cadaver samples were willingly given by donors to the anatomy department of CHUV. Anthropometric measures on these samples complied with Swiss regulation on human studies and did not require formal approval. Formalin-fixated human spinal cords (n 12) were immersed in 0.1 M PBS. The dura was carefully dissected using appropriate surgical tools to identify and expose the lumbosacral spinal segments. The roots were pinned individually using a specific color-code at their entry point to the cord. The length of each lumbosacral spinal segment was measured using a caliper. The length of each spinal segment was defined as the root attachment length plus the lower interroot length. The measurements were averaged over the total number of dissected cords.

Imaging data. Detailed methods for CT, structural MRI and fMRI acquisitions are reported in Supplementary Methods.

Mechanical vibration. MRI-compatible pneumatic vibrators were used to stimulate muscle spindle afferents. Small-amplitude (0.5 mm peak to peak) and constant-frequency (70 Hz) vibrations were delivered using a SMC ITV2050 air-pressure regulator driving the rotation of eccentric ceramic spherical masses embedded in the vibrator turbine. The stimulation parameters were selected based on the fact that small-amplitude vibration activates preferentially primary muscle spindle endings, with responses linearly proportional to the vibration frequency up to 70–80 Hz[54]. A custom software implemented in the LabVIEW environment (National Instruments) allowed to synchronize the vibratory stimulations with the MRI acquisitions. This device did not produce artefacts in the fMRI scans or modify the signal-to-noise ratio, as already reported in previous studies during which vibrations were applied during brain fMRI acquisitions[55,56].

Six pneumatic vibrators were attached to the subject's right leg using elastic bands on the tendons of each pair of agonist/antagonist (extensor/flexor) muscles at the ankle, knee and hip levels. The aim was to target the gastrocnemius medialis/soleus, tibialis anterior, quadriceps, iliopsoas, gluteus and biceps femoris muscles. The protocol was divided in two runs for each pair of agonist/antagonist muscles per joint. In each run, two vibrators, one located on the flexor muscle and the other on the extensor muscle, were alternatively activated in blocks of 10 s. One run consisted of 18 alternating vibration blocks. To avoid any bias, the order of the six runs was randomized.

fMRI data processing. The fMRI preprocessing was carried out using the Functional Magnetic Resonance Imaging of the Brain (FMRIB) Software Library (FSL) v5.0.15 (ref. [57]) and the Spinal Cord Toolbox (SCT) v4.3.16 (ref. [58]).

A two-phase motion correction procedure was performed using FMRIB's Linear Image Registration Tool[59]. First, the volumes of each run were averaged into a mean image. The centerline of the spinal cord was automatically extracted[60]. A cylindrical mask of diameter 30 mm was drawn along it and used to exclude the regions outside the spinal cord. Within each run, all volumes were registered to the mean image using three-dimensional rigid body realignment (spline interpolation and least-squares cost function). To consider that the spinal cord is a nonrigid structure, a two-dimensional slice-wise realignment (spline interpolation and least-square cost function) was conducted, taking as reference the mean image of the corrected volumes[61]. Finally, all runs corresponding to the same session in the scanner were aligned to the first run of the session using three-dimensional rigid body realignment (spline interpolation and least-squares cost function). All images were inspected to ensure that any artefacts or bottom slices with insufficient signal were cropped out. Two slices were in general removed per run. Motion scrubbing was also performed with FSL's tool to identify outliers volumes, using DVARS (the root mean square of the difference of intensity between consecutive volumes) metric in the spinal cord, with a box-plot cutoff (75th percentile 1.5 the interquartile range)[62].

Both the cerebrospinal fluid and the spinal cord were automatically segmented (with manual corrections when necessary) using the SCT[63] from the mean functional and the T2 anatomical images.

Nuisance regressors were built using FSL's physiological noise modelling tool on the acquired cardiac and respiratory signals, using an approach based on the RETROICOR procedure[64]. Low- and high-order Fourier expansions were used to model the physiological signals[65,66]. This resulted in 32 noise regressors, to which an additional cerebrospinal fluid regressor was included (10% most variable cerebrospinal fluid voxels). When no physiological signals were available, regressors based on anatomical priors were determined using component-based noise extraction (aCompCor[67]) through the PhysIO Toolbox[68]. The motion-corrected volumes were masked with the segmented cerebrospinal fluid mask. The first five principal components, as well as the mean of these time series, were extracted and kept as noise regressors.

Coregistration was performed within each subject (functional to anatomical). Using the SCT, functional images were coregistered to the T2 anatomical image with nonrigid transformations.

The motion-corrected functional volumes were spatially smoothed, volume by volume, using a three-dimensional Gaussian kernel (with full width half maximum of 2 2 6 mm ^{3}) along the centerline of the spinal cord to preserve consistency at the anatomical level.

Spinal segments L1 to S2 were identified using the high-resolution structural MRI. The L1 dorsal root was identified from its entry region in the spinal canal (entering just below the L1 vertebra) until the region where it innervates the spinal cord, which defines the L1 spinal segment. The more caudal segments (L2 to S2) were identified by following the dorsal roots along the rostrocaudal axis.

fMRI data analysis. Using the preprocessed functional volumes (motion corrected, smoothed) and the noise regressors (physiological and motion outliers) for each run, a first-level statistical analysis was performed using FMRIB's Improved Linear Model with local auto-correlation correction[69]. As explanatory variables, the timings of the task (block design) were convolved with the three optimal basis functions using FMRIB's Linear Optimal Basis Set[70], with the second and third waveforms orthogonal to the first waveform. The resulting parameter estimates for the two runs were passed through a fixed-effects model to obtain the second level analysis (subject level and task specific) activation maps. To account for multiple comparisons, the Z statistic images were set to (Z 2, P 0.05) whenever possible. These results were then registered to the respective anatomical image to assess their spatial distribution with respect to spinal segments.

Personalized hybrid computational models. We designed a computational framework that supports the semiautomated creation of personalized, geometrically and neurofunctionally realistic hybrid neurophysical volume conductor models of the lower thoracic and lumbosacral spinal cord from high-resolution MRI and CT data. These models combine a three-dimensional finite element method to characterize the electric potential and currents generated by EES with compartmental cable models to estimate the recruitment profile of individual nerve fibers. The detailed methods to generate these models and conduct simulations are reported in Supplementary Methods.

Atlas of computational spinal cord models. Using our computational pipeline, we generated a freely available atlas of 15 personalized computational models from healthy volunteers. The models can be accessed at osparc.io/study/3c62d60a-319d-11ec-8033-02420a0b2de3. These models provided an instrumental resource to analyze the influence of electrode arrangements on the relative recruitment of dorsal roots. We also generated personalized computational models of our study participants. The models for the three participants can be accessed with the following links:

- Participant 1: osparc.io/study/423e27aa-319d-11ec-8033-02420a0b2de3
- Participant 2: osparc.io/study/3f4ea128-319d-11ec-8033-02420a0b2de3
- Participant 3: osparc.io/study/389ac42e-319d-11ec-8033-02420a0b2de3

These models enabled precise preoperative planning that guided the neurosurgical procedure.

Neurosurgical intervention. Laminectomy and paddle lead insertion. An intraoperative tridimensional CT scan (O-Arm version 2, Medtronic) was performed to map the predicted optimal position of the paddle leads to the anatomy of each participant and thus guide the insertion of the leads at this position. An approximately 5-cm midline skin incision was performed, the fascia opened and the muscles retracted bilaterally. Excision of the midline ligamentous structures and laminectomy between L1 and L2 spinal segments enabled the insertion of the paddle leads that were placed over the midline of the exposed dura and advanced rostrally to the target location. Because the 5-6-5 Medtronic lead was narrower and shorter than the new paddle lead, this lead was inserted and tested first. This order minimized possible surgical complications due to the multiple entrances and trajectories within the spinal canal. After the neurophysiological evaluations, the paddle lead was secured by means of bumpy anchors sutured to the ligaments, and a final three-dimensional CT scan was then acquired to register the final position of the paddle lead.

Electrophysiological monitoring. Electrophysiological recordings were conducted using the NIM Eclipse monitoring and stimulation system (Medtronic Xomed, Medtronic). Single pulses of EES (0.5 Hz) were delivered at increasing amplitude to elicit muscle responses that were recorded from subdermal (Neuroline Twisted Pair Subdermal, 12 0.4 mm, Ambu A/S) or intramuscular needle electrodes (Ultra Sharp, 44 mm/27 g, Chalgren Enterprises).

Intraoperative comparison of the paddle leads. During the surgical intervention, the Specify 5-6-5 paddle lead (Specify 5-6-5, Medtronic) was inserted before the new paddle lead. Electrophysiological monitoring of muscle responses guided the placement to an optimal position to recruit the iliopsoas muscle (L1 dorsal root). Recordings were obtained at three different positions apart from 2 mm, centered on the optimal position. Then, the new paddle lead (ONWARD Medical) was inserted through the same opening. The same procedure was then repeated. Because the new paddle lead displayed superior selectivity compared with the Specify 5-6-5, the new paddle lead was implanted chronically.

Paddle array. The new paddle array was fabricated using conventional biomedical technologies. Extensive bench and in vivo testings were conducted to validate the mechanical, electrical and biocompatibility properties of the paddle lead, which led to the equivalent of an investigational device exemption from Swiss competent authorities.

Pulse generator implantation. An IPG (Medtronic Activa RC, Medtronic) commonly used for deep-brain stimulation therapies was inserted into a subcutaneous pocket in the participant's abdomen. The paddle array cables were then tunneled between both openings and connected to the IPG.

Configuration of activity-specific stimulation programs. After approximately 10 days of rest after surgery, participants started a 1-month period during which we configured activity-specific stimulation programs to support the performance of motor activities involving leg and trunk musculatures.

Electrode configurations. We delivered EES with electrode configurations targeting the dorsal roots projecting to the spinal cord regions containing the motor neuron pools associated with the intended movement. These spinal cord regions were derived from the projectome of proprioceptive neurons innervating the homonymous motor neurons, as identified with fMRI recordings. The cathodes were selected based on intraoperative recordings at the final position of the paddle lead. Additional anode configurations completed the cathodes to increase the selectivity when necessary. The procedure to elaborate the library of anodes and cathodes is described in Extended Data Fig. 6. EES pulse width was fixed at 300 s. The amplitude and frequencies of EES were optimized for each electrode configuration, as described in Extended Data Fig. 7.

Spatiotemporal stimulation sequences to support walking. Sequences of EES pulses to support walking were derived from the spatiotemporal maps of motor neuron activation reconstructed from muscle activity of healthy individuals during walking[8]. These spatiotemporal maps revealed that walking involves the successive activation of three hotpots restricted to specific spinal cord regions. We thus created a template of spatiotemporal stimulation sequences that aim to reproduce the spatiotemporal activation pattern of these hotspots during walking in healthy individuals. For each targeted hotspot, we selected an appropriate anode/cathode configuration from the library and updated the template with these configurations. The parameters (frequency, amplitude), onset and duration of each train of EES were optimized during walking on treadmill and overground and by inspecting the synchronicity of the muscular activity and kinematics with EES trains and integrating the feedback from the physical therapist and participant, as detailed in Extended Data Fig. 7.

Spatiotemporal stimulation sequences to support other motor activities. We then configured activity-specific stimulation programs to support other motor activities such as standing, cycling, sit-to-stand, leg press and swimming. For this purpose, we exploited the same framework as for elaborating the stimulation template for walking. We thus conceived spatiotemporal sequences that reproduce the natural activation of motor hotpots/muscle groups during each motor activity. We also developed EES programs that targeted the motor neurons innervating the trunk and abdominal musculatures to facilitate trunk postures and the execution of trunk exercises. This procedure is described in Extended Data Fig. 9.

Clinical evaluations. ISNCSCI. Each participant's neurological status was assessed based on the ISNCSCI, a comprehensive clinician-administered neurological examination of residual sensory and motor function quantifying SCI severity[53].

Six-minute walk test. Endurance was assessed by the distance covered overground within 6 min with a standard four-wheel walker and spatiotemporal EES turned on. This test was performed at the beginning and at the end of the 5 months of rehabilitation.

Quantification of muscle mass. Muscle mass was quantified from non-contrast CT images obtained with a 64-detector row CT scanner (Discovery CT750 HD, GE Healthcare) at the abdominal (L3 vertebra) and mid-thigh (25 cm cranial to the tibiofemoral joint space) levels, acquired before surgery and after the period of 5 months of rehabilitation. Muscle segmentations were performed semiautomatedly in ImageJ by applying specific CT number thresholds (in Hounsfield units (HU)) for the identification of muscle (from 29 to 150 HU) and adipose (from 190 to 30 HU) tissues [71]. Muscle mass and skeletal muscle area are reported (in cm^2) for specific abdominal and thigh muscles or muscle compartments.

Rehabilitation program. Participants followed a rehabilitation program four to five times per week for 5 months. The rehabilitation program was personalized to participants' performance. This period of rehabilitation comprised walking on a treadmill and overground with multiple assistive devices, sit-to-stand, standing, leg and trunk muscle exercises, swimming and cycling. Activity-specific stimulation programs were delivered to enable the practice of these activities.

Technological framework. Rehabilitation and movement analysis environment. When necessary, a tailored amount of body weight support was provided to the participants using an overhead support system based on cable robot technology (Rysen, Motek Medical BV). This robotic system allows the application of tailored forces to the trunk through a dedicated harness along the vertical and anteroposterior directions.

Electromyographic activity of selected muscles was acquired at a 2-kHz sample rate using the 16-channel wireless Delsys system, with bipolar surface electrodes placed over the muscles of the lower limbs (iliopsoas, rectus femoris, adductors, vastus lateralis, semitendinosus, tibialis anterior, medial gastrocnemius and soleus) and/or trunk muscles (abdominal muscles, quadratus lumborum and obliques). Kinematic recordings were obtained at a 100-Hz sampling rate using a three-dimensional motion capture system (Vicon Motion Systems and Nexus v1.8.5 software), consisting of 14 infrared cameras that covered a 12 4 2.5 m workspace. Body kinematics were captured by these infrared cameras through the use of infrared-reflective markers positioned over standardized anatomical landmarks. We also captured chronophotographic images of participants using a high-definition camera (FUJIFILM X-T2, five images/s, ISO 6400, shutter speed 1/250 s). Successive snapshots were overlaid offline to illustrate the dynamic of movements.

Neurostimulation system. EES was delivered with an IPG (Medtronic Activa RC) that enabled monopolar and multipolar stimulation at constant current or constant voltage through one or a subset of the 16 electrodes of the paddle lead or the case of the IPG (anode). The IPG was modified from its clinical version with an investigational firmware that enabled real-time communication with a software running on an external computer (NEUWalk Research Programmer Application (NRPA), model 09103, Medtronic). The NRPA acted as a relay between EES-triggering commands sent by the control software, G-Drive Plus (described below), and the IPG. The NRPA communicated wirelessly with the IPG through the following communication chain: the NRPA sent commands via a virtual COM port corresponding to a Bluetooth adapter, a custom wireless bridge consisting of a nano computer (Raspberry Pi) received this command and forwarded it to a virtual COM port 6 corresponding to a USB adapter, a USB to infrared adapter (ACT-IR224UN-LN115-LE, ACTiSYS) transformed this command into infrared signals that were then read by a modified Medtronic patient's programmer (Sensing Programmer Telemetry Module, Medtronic), which finally transmitted the command to the patient's IPG by electromagnetic induction through the skin (Supplementary Fig. 1).

Software App for configuration, optimization and evaluation of neurostimulation. A custom software application (App) was built to configure, optimize and evaluate the effects of EES (Supplementary Fig. 1). The C# App runs on a desktop computer, laptop or tablet and interfaces with the stimulation system (through the NRPA App) and sensor systems for data acquisition and closed-loop stimulation. The software includes a stimulation scheduler that enables the rapid personalization of spatiotemporal stimulation sequences from preprogrammed templates. The user can choose to loop a sequence automatically, switch between different motor activities with one click or link stimulation sequences to specific events detected by the sensors. These events can be triggered by detecting movement-specific changes detected through inertial measurement units (IMUs) (NGIMU, x-io Technologies Limited) placed on the participant's body or by clicking on custom-built ergonomic buttons mounted on an assistive device and connected to the analog input ports of the IMUs. The IMUs are connected with the software App through Wi-Fi, streaming quaternion or analog input data at 30 Hz. For movement detection, quaternion values are converted into Euler angles indicating the angular positions of the trunk or limbs, depending on the location of the IMUs. Movement-specific events are triggered when these angles cross user-defined and movement-specific thresholds in a predefined direction. The software provides real-time visualization (SciChart WPF library, SciChart) of the muscular activity and leg kinematics based on wireless sensors that measures the electromyographic activity and IMUs placed on the participant's body (Delsys Trigno System, Delsys Incorporated). The App also triggers acquisition from video cameras. The muscular and kinematic data are synchronized with the stimulation sequences and color-coded with respect to the targeted motor hotspots. This color-coded visualization allows the immediate assessment of the effects of the stimulation on muscle activity and whole-body kinematics. All the acquired data, including the information about EES stimulation patterns, are saved for offline analysis.

The App provides graphical interfaces tailored to the needs of the different user types (i.e. stimulation experts, physical therapists and study participants). Concretely, the same App can be used by stimulation experts on a multiscreen desktop system to configure and optimize stimulation parameters, therapists to select and modulate rehabilitation exercises on a handheld tablet or study participants to start and stop activity-dependent stimulation programs to support activities of daily living through a smartwatch.

Data processing. Analysis of intraoperative muscle activity. Intraoperative recordings of muscle activity were band-pass filtered between 10 and 450 Hz (fourth-order Butterworth filter). The peak-to-peak amplitudes of the monosynaptic components of muscle responses were extracted and normalized with respect to the maximal value obtained during the recordings.

Analysis of lower limb muscle activity. The electromyographic activity from lower limb muscles was processed according to SENIAM (Surface Electromyography for the Non-Invasive Assessment of Muscles) standards for electromyographic recordings. All displayed electromyographic activities during walking were band-pass filtered between 10 and 450 Hz (fourth-order Butterworth filter). A moving average of the rectified electromyographic signal within a centered 250-ms time window was used to generate normalized electromyographic envelopes for quantification.

Recruitment of trunk and abdominal muscles during single-pulse EES. Electromyographic signals from trunk abdominal muscles were band-passed filtered between 10 and 450 Hz (fourth-order Butterworth filter. EES onset was determined using semiautomatic methods based on recordings of stimulation artefacts. The temporal window of muscle responses was defined within 40 or 50 ms starting 10 ms after EES onset, depending on the muscle. For each amplitude of EES, muscle responses were quantified as the peak-to-peak amplitude. These values were translated into recruitment curves that we displayed in circular plots. In these circular plots, muscles are distributed at different angular positions. The radial axis corresponds to EES amplitude (Extended Data Fig. 8). A color shading reports the normalized amplitude of muscle activity. The black circle highlights the EES amplitude that corresponds to the highest selectivity index. The polygon describes the muscle selectivity at the optimal EES amplitude; the edges of the polygon represent the normalized muscle activity on the radial axis for a particular muscle, scaled so that the polygon fills the circle.

Analysis of trunk kinematics. Reflective markers were secured to the spine at T10 and L5, and on both knees to record trunk and leg kinematics. The responses were analyzed over the window of 500 ms that followed the onset of the stimulation. Kinematic data were low-pass filtered (fourth-order Butterworth filter) with a cutoff at 10 Hz.

Analysis of trunk posture and kinematics during exercises. Trunk exercises were recorded with a FujiFilm XT-2 camera. Video-based kinematic analysis of the lumbar curvature was performed through a semiautomated detection of the body segments and by an expert visually fitting circles to calculate the lumbar curvature.

Statistics. All quantifications show the mean and all individual data. Comparisons between two conditions were performed using a two-tailed Student's t test when normality was confirmed or a nonparametric Mann–Whitney rank sum test otherwise. Comparisons involving more than two categories were performed using a one-way analysis of variance, followed by the post-hoc Tukey's honestly significant difference tests (*P 0.05; **P 0.01; ***P 0.001).

Reporting Summary. Further information on research design is available in the Nature Research Reporting Summary linked to this article.

Data availability

Data that supports the findings are available in the following data depository: https://doi.org/10.5281/zenodo.5614586 Source data are provided with this paper.

Code availability

Software routines developed for the data analysis will be made available upon reasonable request to gregoire.courtine@epfl.ch.

References

53. Kirshblum, S. & Waring, W. Updates of the International Standards for Neurologic Classification of Spinal Cord Injury. Phys. Med. Rehabil. Clin. N. Am. 25, 505–517 (2014).
54. Roll, J. P. & Vedel, J. P. Kinaesthetic role of muscle afferents in man, studied by tendon vibration and microneurography. Exp. Brain Res. 47, 177–190 (1982).
55. Landelle, C., Ahmadi, A. E. & Kavounoudias, A. Age-related impairment of hand movement perception based on muscle proprioception and touch. Neuroscience 381, 91–104 (2018).
56. Kavounoudias, A. et al. Proprio-tactile integration for kinesthetic perception: an fMRI study. Neuropsychologia 46, 567–575 (2008).
57. Jenkinson, M., Beckmann, C. F., Behrens, T. E. J., Woolrich, M. W. & Smith, S. M. FSL. Neuroimage 62, 782–790 (2012).
58. Leener, B. D. et al. SCT: Spinal Cord Toolbox, an open-source software for processing spinal cord MRI data. Neuroimage 145, 24–43 (2017).
59. Jenkinson, M., Bannister, P., Brady, M. & Smith, S. Improved optimization for the robust and accurate linear registration and motion correction of brain images. Neuroimage 17, 825–841 (2002).
60. Gros, C. et al. Automatic spinal cord localization, robust to MRI contrasts using global curve optimization. Med. Image Anal. 44, 215–227 (2018).
61. Cohen-Adad, J. et al. Venous effect in spinal cord fMRI: insights from intrinsic optical imaging and laser speckle. Neuroimage 47, S186 (2009).
62. Power, J. D. et al. Methods to detect, characterize, and remove motion artifact in resting state fMRI. Neuroimage 84, 320–341 (2014).
63. Gros, C. et al. Automatic segmentation of the spinal cord and intramedullary multiple sclerosis lesions with convolutional neural networks. Neuroimage 184, 901–915 (2019).
64. Eippert, F., Kong, Y., Jenkinson, M., Tracey, I. & Brooks, J. C. W. Denoising spinal cord fMRI data: approaches to acquisition and analysis. Neuroimage 154, 255–266 (2017).
65. Brooks, J. C. W. et al. Physiological noise modelling for spinal functional magnetic resonance imaging studies. Neuroimage 39, 680–692 (2008).
66. Kong, Y., Jenkinson, M., Andersson, J., Tracey, I. & Brooks, J. C. W. Assessment of physiological noise modelling methods for functional imaging of the spinal cord. Neuroimage 60, 1538–1549 (2012).
67. Behzadi, Y., Restom, K., Liau, J. & Liu, T. T. A component-based noise correction method (CompCor) for BOLD and perfusion-based fMRI. Neuroimage 37, 90–101 (2007).
68. Kasper, L. et al. The PhysIO Toolbox for modeling physiological noise in fMRI data. J. Neurosci. Meth. 276, 56–72 (2017).
69. Woolrich, M. W., Ripley, B. D., Brady, M. & Smith, S. M. Temporal autocorrelation in univariate linear modeling of FMRI data. Neuroimage 14, 1370–1386 (2001).
70. Woolrich, M. W., Behrens, T. E. J. & Smith, S. M. Constrained linear basis sets for HRF modelling using variational Bayes. Neuroimage 21, 1748–1761 (2004).
71. Gomez Perez, S. L. et al. Measuring abdominal circumference and skeletal muscle from a single cross sectional computed tomography image. Jpen-parenter. Enter. 40, 308–318 (2016).
72. Schirmer, C. M. et al. Heuristic map of myotomal innervation in humans using direct intraoperative nerve root stimulation. J. Neurosurg. Spine 15, 64–70 (2011).

Acknowledgements

We thank our study participants for their commitment and trust. All participants gave their informed consent for publication of their images. We thank A. Curt for support; A. van der Kolk and F. Visser for support in imaging data collection and inspection; and many students, interns and former employees for various contributions, including R. Wang, C. Puffay, Y. L. R. Wan, I. Perret, E. Revol, M. Van Campenhoudt, I. Youssef,

I. Turcu, F. Sellet, G. Carparelli, C. Moerman, D. Scherrer-Ma, F. Magaud, M. Damiani and N. Regazzi. Investigational implantable stimulators and paddle leads were donated by Medtronic and ONWARD Medical. This work was supported by Wings for Life, the Defitech Foundation, the International Foundation for Research in Paraplegia, Rolex for Enterprise, Carigest Promex, Riders4Riders, ALARME, the Panacée Foundation, the Pictet Group Charitable Foundation, the Firmenich Foundation, ONWARD Medical, European Union's Horizon 2020 (785907 Human Brain Project SGA2), RESTORE: Eurostars E10889, CONFIRM!: Eurostars E!12743, the Swiss National Science Foundation (NCCR Robotics), the European Research Council (ERC-2015-CoG HOW2WALKAGAIN 682999), the Commission of Technology and Innovation Innosuisse (CTI 41871.1 IP_LS and CTI 25761.1) and the H2020-MSCACOFUND-2015 EPFL fellows program (grant 665667 to F.B.W.).

Author contributions

E.B., S.D.H.-C. and E. Paoles contributed equally. A.R., S.K., R.D., E.B., F.B., J.R., M.D., C.V., L. McCracken, N. Hankov, M.V., L.B.-F., H. Lorach, A.G., E. Pralong, M.R., K.M., Q.B., L.A., F.B.W., J. Bloch and G.C. performed experiments and analyzed data. A.R., S.K., R.D., H.M., A.C., B.L., T.N., M.D., N. Hankov, M. Caban, L.B.-F., C.H., S.B., S.C., N.G., B.F., N.B., T.D., D.G., J.B., K.M., E.K., N.K., E.N., M. Capogrosso, F.B.W., J. Bloch and G.C. designed, developed and/or fabricated hardware and/or software. A.R., S.D.H.-C., E. Paoles, H.M., A.C., B.L., T.N., S.B., S.C., N.G., N.K., E.N. and M. Capogrosso performed simulations. A.R., E.B., S.D.H.-C., E. Paoles, F.B., N.K., J.-B.L., E.F., S. Mandija, L. Mattera, R.M., B.N., M.F., A.K., S. Mandija, C.A.T.v.d.B. and D.V. acquired medical imaging datasets. E.B., A.P., M.T., N. Herrmann, M.W., L.G., I.F., V.R., K.K. and G.E. conducted physical therapy. R.D., M.V., A.W., C.J., L.B-F., R.B., V.D., H. Lambert and L.A. managed regulatory affairs. C.W. handled intellectual property. A.R., S.K., R.D., E.B., S.D.H.-C., J.R., L.A. and G.C. prepared illustrations. J. Bloch performed neurosurgical interventions. G.C. and J. Bloch conceived and supervised the study. G.C. wrote the paper, and all the authors contributed to its editing.

Competing interests

G.C., J. Bloch, S.M., K.M., F.B.W. and M.Capogrosso hold various patents in relation with the present work. V.D., D.G., J. Bakker, H.L., A.W., C.J., M.D., M. Caban and E. Paoles are ONWARD Medical employees. G.C. is a consultant with ONWARD Medical. G.C., J. Bloch, S.M. and V.D. are shareholders of ONWARD Medical, a company with direct relationships with the presented work. N.K. and E.N. are shareholders of ZMT Zurich MedTech AG, which produces the Sim4Life software. C.W. handles intellectual property for ONWARD Medical. The remaining authors declare no competing interests.

Additional information

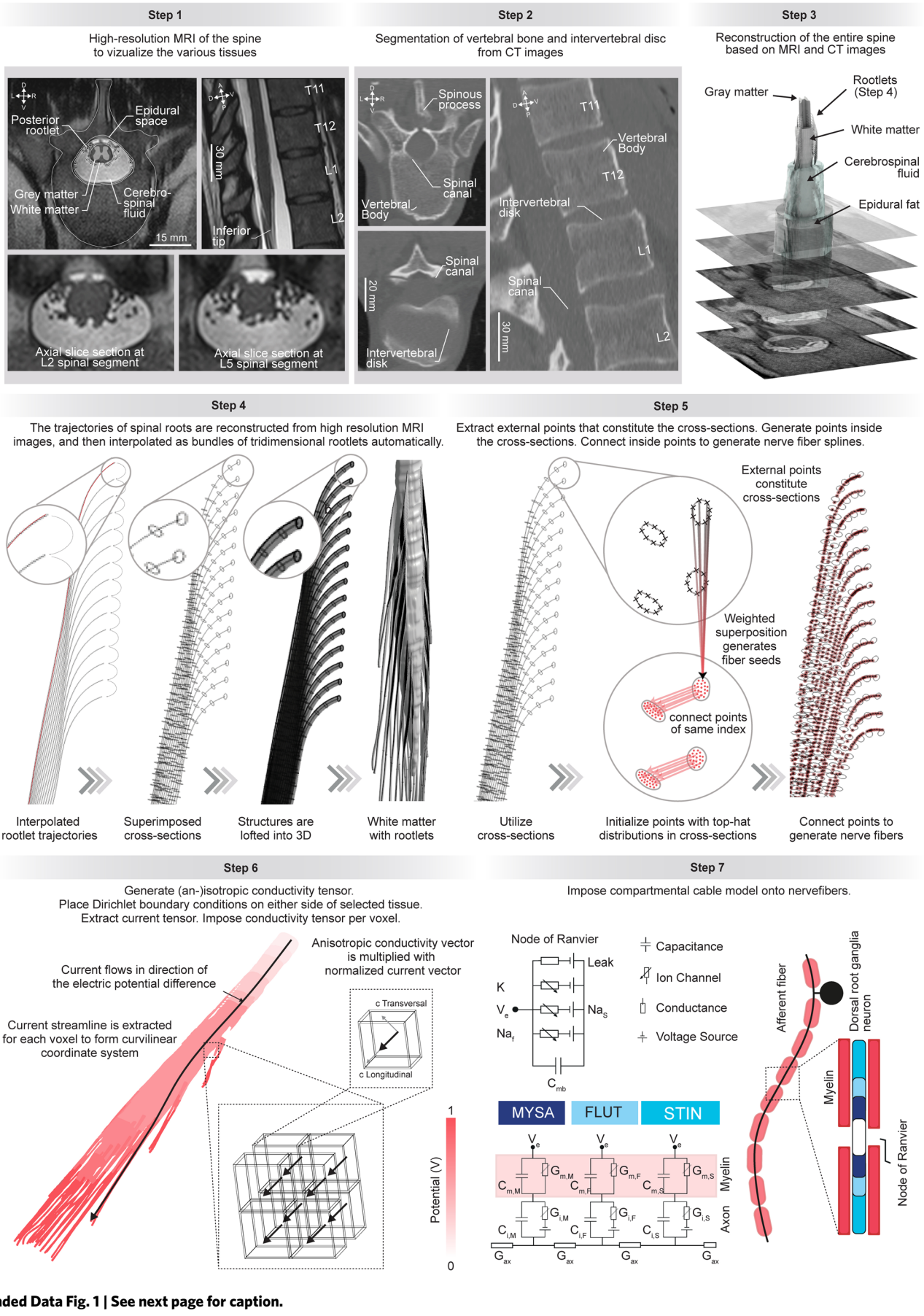
Extended data is available for this paper at https://doi.org/10.1038/s41591-021-01663-5.

Supplementary information The online version contains supplementary material available at https://doi.org/10.1038/s41591-021-01663-5.

Correspondence and requests for materials should be addressed to Jocelyne Bloch or Grégoire Courtine.

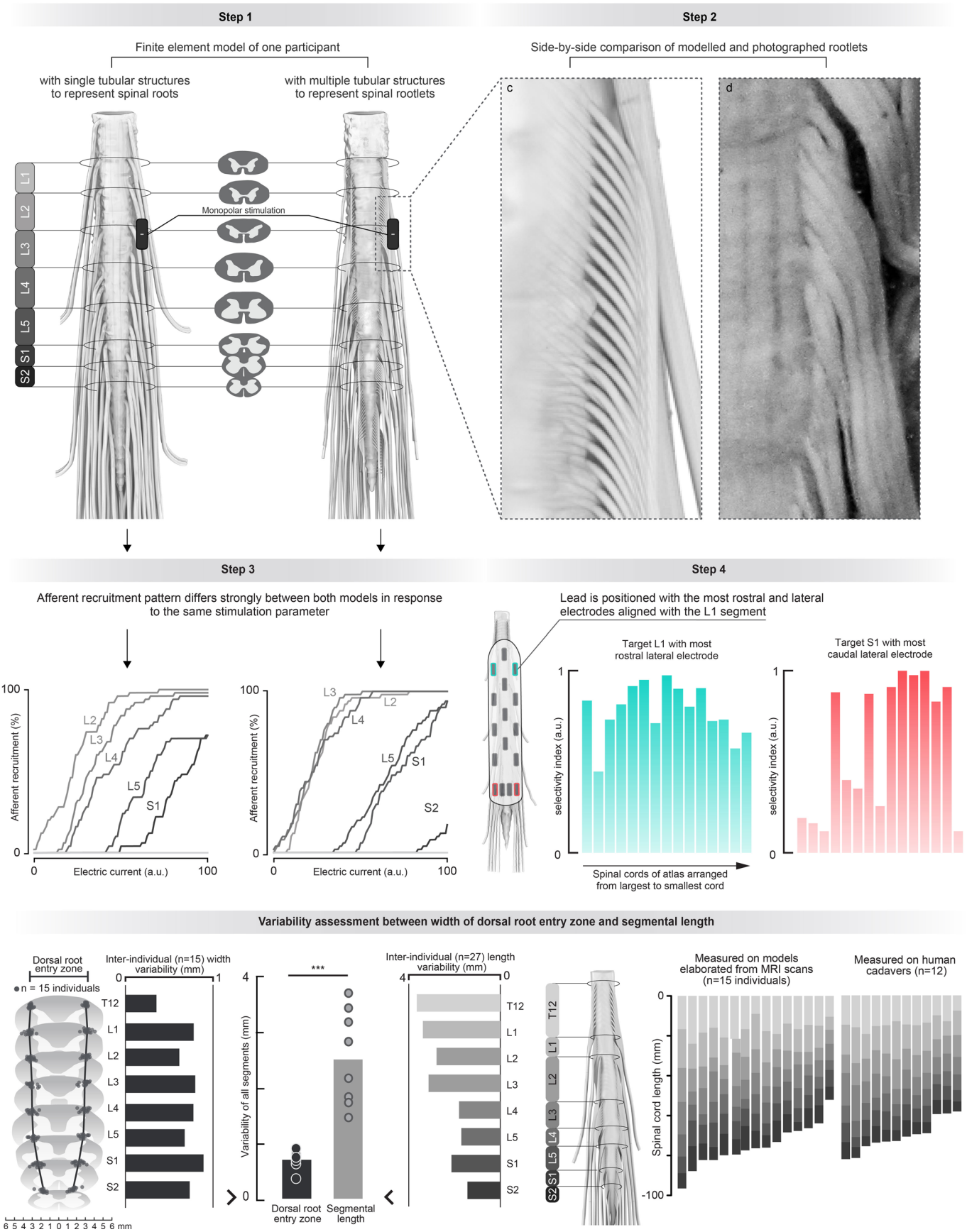
Peer review information Nature Medicine thanks Bruce Dobkin, Philip Star, Blair Calancie and the other, anonymous, reviewer(s) for their contribution to the peer review of this work. Jerome Staal was the primary editor on this article and managed its editorial process and peer review in collaboration with the rest of the editorial team.

Reprints and permissions information is available at www.nature.com/reprints.



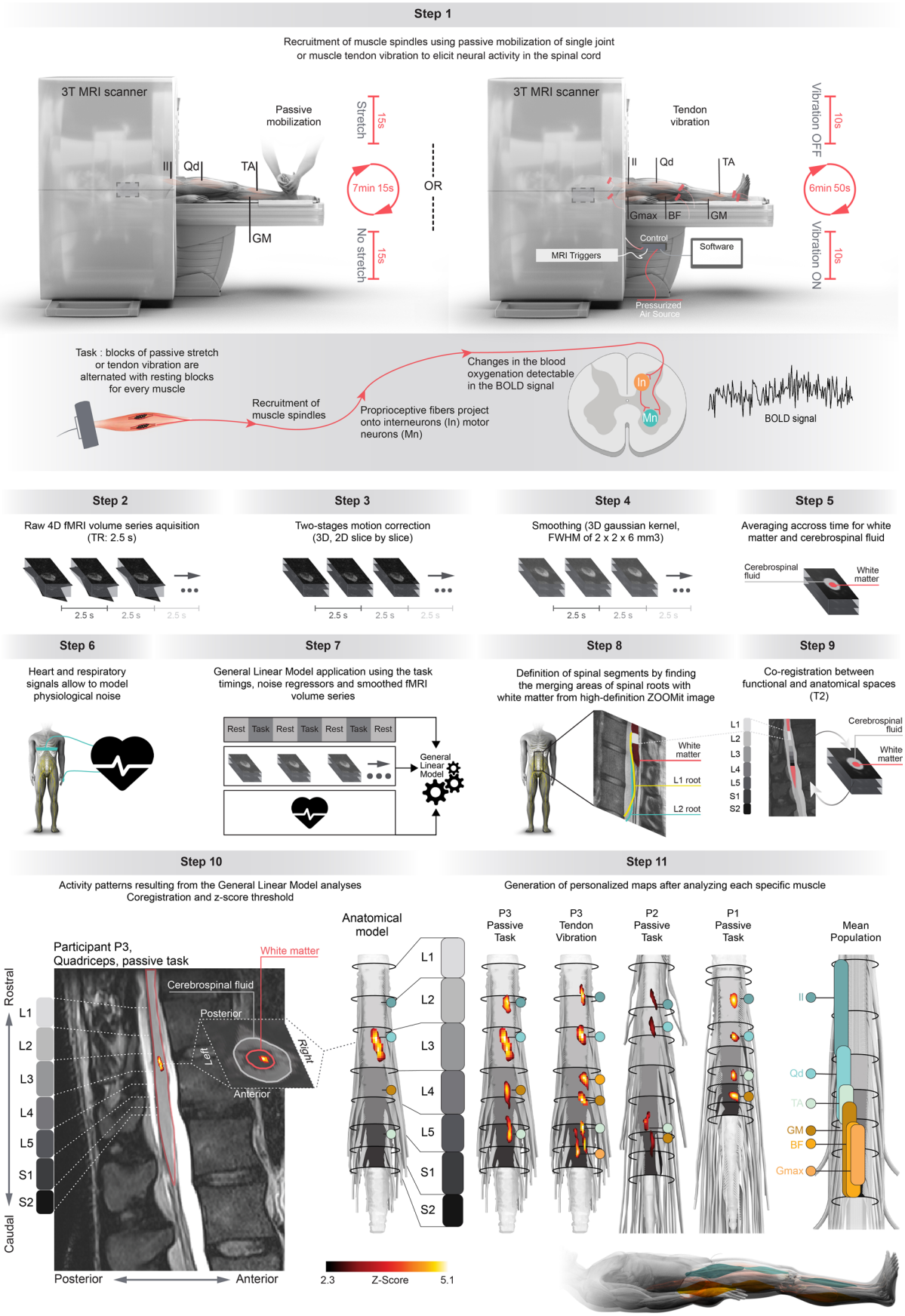
Extended Data Fig. 1 | See next page for caption.

Extended Data Fig. 1 | Personalizable computational models of the interactions between EES and the spinal cord. Step 1, High-resolution MRI images enable clear-cut visualization of spinal tissues, including individual dorsal roots. **Step 2**, CT images enable reconstructing the tridimensional geometry of vertebral bodies. **Step 3**, Elaboration of highly realistic anatomical models from MRI and CT scans. **Step 4**, Automatic generation of rootlets based on the identification of the uppermost rootlet (shown in red) in high-resolution MRI acquisitions. Rootlet trajectories are interpolated from this rootlet, using the measured segment length as a reference. **Step 5**, Splines representing the nerve fibers are automatically generated inside the rootlets. For this purpose, points are initialized in each cross-section based on a weighted superposition of the points constituting the cross-section itself. These points are connected to generate splines. **Step 6**, Conductivity maps are imposed on each voxel of the discretized finite element models. The white matter and rootlets require an anisotropic conductivity map. Functionality has been implemented in Sim4Life for that purpose that generates anisotropic conductivity maps by solving a diffusion problem with suitable boundary conditions in the tissues of interest and locally aligning conductivity tensors with the gradient of the obtained solution. **Step 7**, Compartmental cable models are initialized along each spline to integrate the nerve fibers.



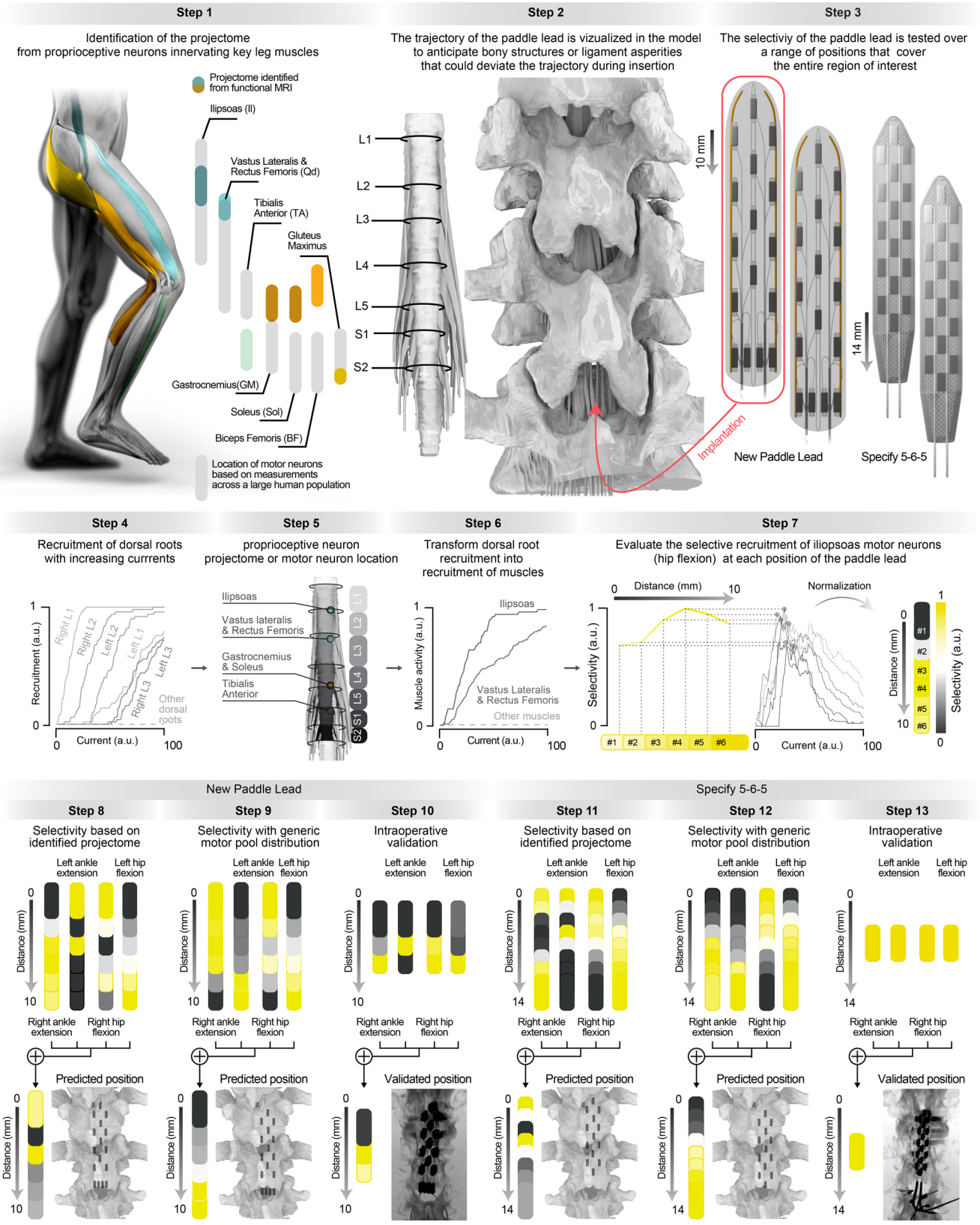
Extended Data Fig. 2 | See next page for caption.

Extended Data Fig. 2 | Importance of modeling rootlet bundles. Step 1, Models of the same spinal cord wherein the dorsal roots are modelled as single tubular structures (left) versus multiple tubular structures mimicking the topology of rootlet bundles observed in humans (right), as shown in **Step 2**, side by side comparison of the rootlet bundles in the model and in a real spinal cord. To create the model of the rootlets, we determined the entry point of the uppermost rootlet for each spinal segment, and then populated the space from the uppermost rootlet of a given dorsal root to the uppermost rootlet of the next dorsal root by distributing rootlets homogeneously across this space. **Step 3**, A pulse of EES was delivered with increasing intensities through the electrode depicted in step 1, over the L3 dorsal root. The plots show the resulting recruitment curve of each dorsal root. The explicit models of rootlets led to pronounced differences in the recruitment curves of each dorsal root. **Step 4**, Performance of the new paddle lead evaluated in 15 computational models of the atlas. The top left electrode of the paddle lead was positioned over the dorsal root innervating the L1 spinal segment, as depicted in the model on the left. The plot on the left reports the selectivity of this electrode for each model, organized laterally based on the length of the spinal cord (as reported in Fig. 1). The plot on the right reports the selectively of the bottom left electrode to recruit the dorsal root projecting to the S1 spinal segment. **Lower Panel**, Horizontal bar plots on the left report the variability of the width of the dorsal root entry zone (n 15 healthy volunteers). Horizontal bar plots on the right report the variability of length of each spinal segment (n 27 spinal cords). The bar plot between these two plots reports the variability of the width of the dorsal root entry zones and of the length of spinal segments. p 0.000035, ***, P 0.0001, two-tailed t-test.



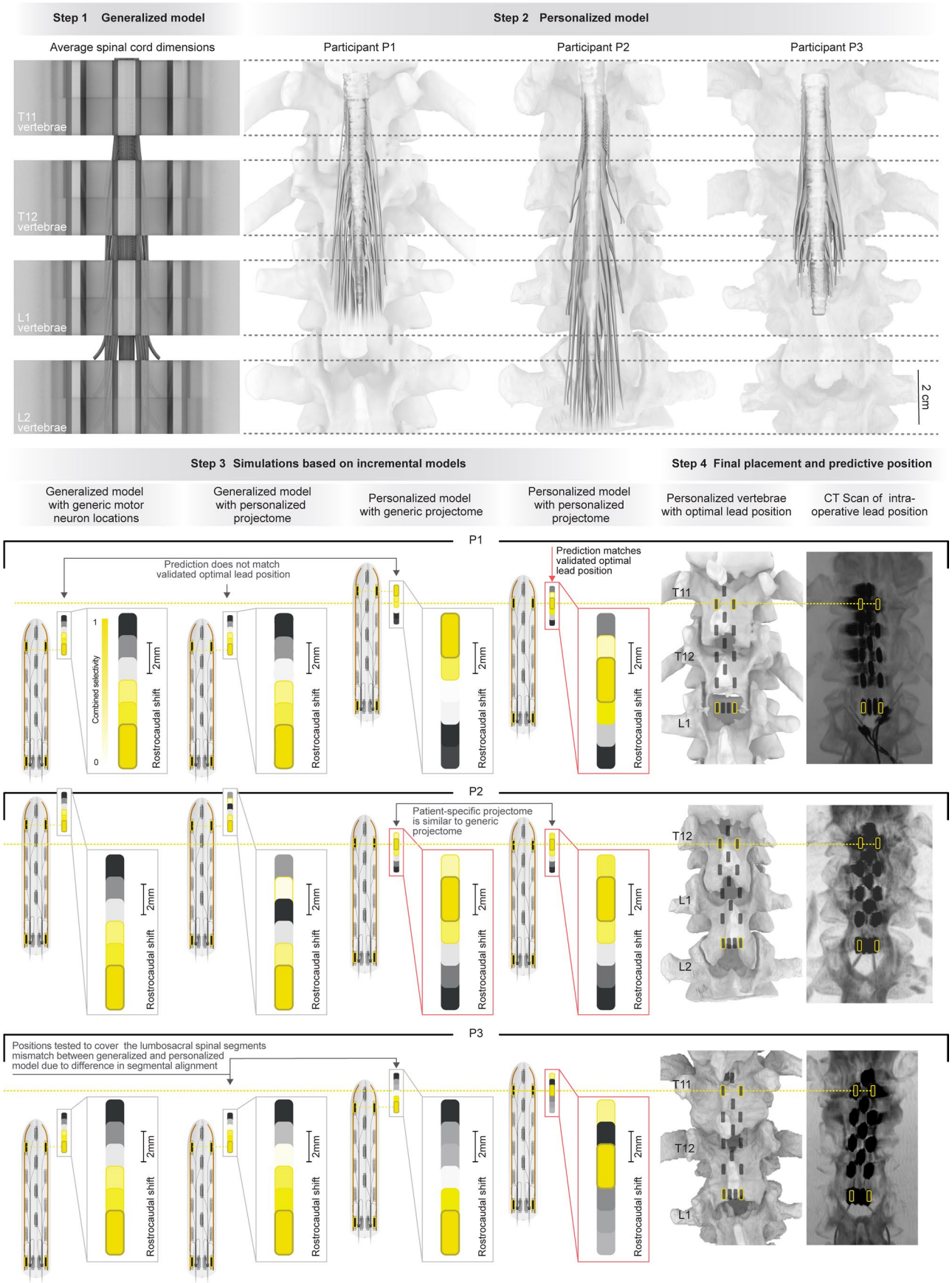
Extended Data Fig. 3 | See next page for caption.

Extended Data Fig. 3 | Identification of the projectome from propriospinal neurons. Step 1, Acquisition of functional MRI from the spinal cord in response to the recruitment of proprioceptive afferents from specific leg muscles. The muscle spindles are recruited either by stretching the muscles in which they are embedded (the limb is mobilized by a physiotherapist, aided with audio cues), or by applying muscle tendon vibration using MR-compatible pneumatic vibrators (synchronized with MRI triggers). Two runs are acquired for each muscle. Only the right leg muscles are tested. In addition to the functional volume series, T2 anatomical images and physiological (heart rate, respiratory) signals are acquired. **Step 2**, Raw fMRI volume series are repeatedly acquired every 2.5 s (TR) in functional runs lasting about 7 minutes. **Step 3**, A two staged motion correction (3D and then 2D slice-by-slice) is applied for each run. First, the volumes are registered to their respective averaged-in-time image using 3D rigid body realignment. Secondly, taking as reference the averaged-in-time corrected volume, a slice-by-slice 2D realignment is applied thus accounting for the nonrigid property of the spinal cord. **Step 4**, The motion-corrected series are spatially smoothed, volume by volume with 3D gaussian kernel with full width at half maximum (FWHM) of 2 2 6 mm ^{3}. **Step 5**, The motion-corrected series are again averaged through time. The cerebrospinal fluid and white matter are segmented from this mean functional image. **Step 6**, Physiological signals (heart rate and respiratory) acquired concomitantly to the fMRI volumes are used to model physiological noise (RETROICOR based procedure). If no signals are available, noise regressors are built with component based noise extraction (aCompCor). **Step 7**, Acquisition timings corresponding to the task-design, pre-processed (motion corrected, smoothed) fMRI volume series and physiological noise regressors are submitted to a specific first level generalized linear model. A second level fixed effects analysis (subject level, task specific) is performed by combining the two runs. Whenever possible, multiple comparison corrections are performed (Z 2, p $_{corr}$ 0.05). **Step 8**, Spinal segments are identified from high-definition T2-ZOOMit structural images that allow visualization of the dorsal roots. Spinal segments are then reported in the T2 anatomical image acquired in each run. **Step 9**, Using non-rigid transformations, the mean functional images are co-registered to the T2 anatomical image. **Step 10**, Thresholded activity patterns resulting from the generalized linear model are coregistered to the anatomical image. The projectome of proprioceptive neurons innervating the mobilized muscles are extracted and mapped to the anatomical model. **Step 11**, Projectomes from the three participants, and for comparison, averaged myotome distribution measured electrophysiologically in a large population of patients undergoing surgery. The color dots represent the reconstructed projectome from key leg muscles. Vertical color bars represent mean population distribution of muscular motor hotpots. The projectomes differed across the participants. In particular, the projectome identified in P3 revealed an unexpected inversion of the projectome from ankle antagonists. This rostrocaudal inversion was confirmed electrophysiologically.



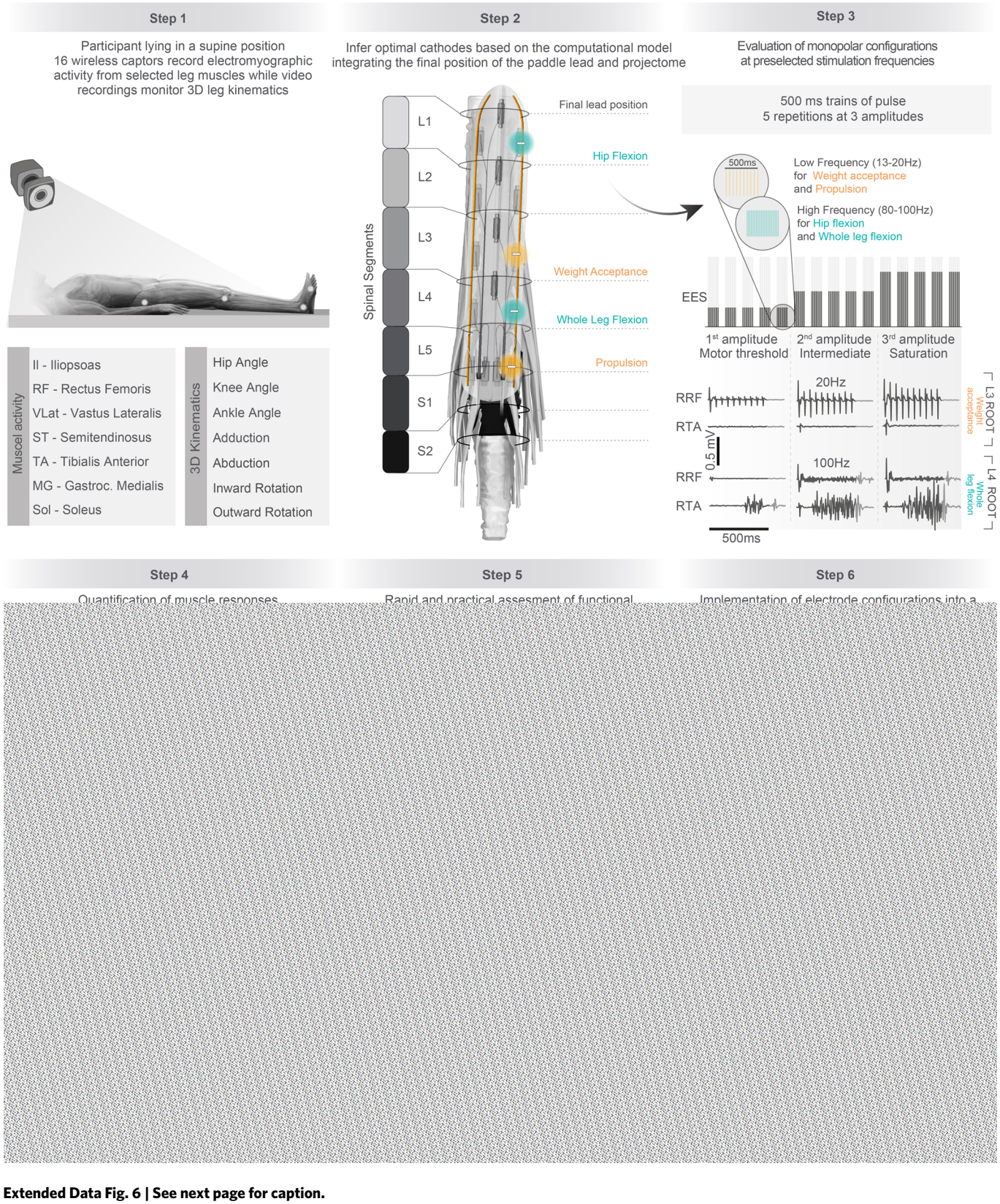
Extended Data Fig. 4 | See next page for caption.

Extended Data Fig. 4 | Preoperative planning for optimal placement of the new paddle lead. Step 1, CT, structural MRI and functional MRI acquisitions allow to personalize a computational model of the interactions between EES and the spinal cord for each participant. **Step 2**, The insertion of the new paddle lead within the spinal canal is visualized in the model to anticipate bony structures or ligaments that could deviate the trajectory. **Step 3**, The new paddle lead is positioned at 6 locations separated by 2 mm, thus covering the entire region of the spinal cord targeted by the therapy. The same procedure was applied to the Specify 5-6-5 lead, except that 2 additional locations were necessary to cover the entire region since this lead is shorter than the new paddle lead. **Step 4**, The plot shows the recruitment of each dorsal root when simulating the delivery of EES at increasing intensities through the top left electrode of the paddle lead. The same simulations were performed for the electrodes located at each corner of the paddle lead. **Step 5**, The recruitment of dorsal roots is translated into the recruitment of motor pools based on a transformation matrix that maps the recruitment of afferents to the recruitment of motor pools. The transformation matrix was either based on the averaged location of motor pools across the human population[72], or the projectome of proprioceptive neurons from key leg muscles identified from functional MRI. **Step 6**, Applying the transformation matrix depicted in Step 5 allows to convert the predicted recruitment of dorsal roots shown in Step 4 into a prediction of motor pool recruitment. **Step 7**, For each position of the lead, the recruitment of the targeted motor pools compared to the non-targeted motor pools is measured to obtain a selectivity index. For example, the recruitment of the dorsal root projecting to the L1 spinal segments intends to recruit the motor neurons innervating the iliopsoas muscle to elicit hip flexion. The relative recruitment of the iliopsoas muscle versus the rectus femoris or vastus lateralis muscles is transformed into a selectivity index. For each position of the paddle lead, the selectivity index for the tested electrode is color coded, and the selectivity between the tested locations interpolated to obtain a continuum. **Step 8**, The selectivity indices obtained for the electrodes located at each corner of the paddle lead (from left to right, targeting motor neurons eliciting hip flexion or ankle extension) are aggregated into a combined selectivity index that defines the performance of the paddle lead at the tested position. The optimal position for the paddle lead was defined as the position for which the highest combined selectivity index was obtained (most yellow rectangle). **Step 9**, Optimal position of the new paddle lead predicted based on a personalized computational model but a generic distribution of motor neuron locations. **Step 10**, Intraoperative quantification of the combined selectivity index, and thus identification of the optimal position of the new paddle lead. The predicted optimal position of the paddle lead based on a personalized model with the identified projectomes of proprioceptive neurons matched the optimal position validated intraoperatively, whereas simulations based on the averaged location of motor pools across the human population failed to predict the optimal position. **Step 11-13**, The procedures described in Steps 8-10 were repeated for the Specify 5-6-5 paddle lead. Note that the intraoperative validation of the optimal position of the Specify 5-6-5 was restricted to one position to minimize the duration of the surgical intervention.



Extended Data Fig. 5 | See next page for caption.

Extended Data Fig. 5 | Impact of model abstractions to determine the optimal position of the paddle lead. Step 1, Generalized computational model of the interaction between EES and the spinal cord, including the location of motor neurons from key leg muscles. **Step 2**, Personalized computational model of the interaction between EES and the spinal cord for the three participants. The models are aligned with the generalized model depicted in Step 1. **Step 3**, Simulations predict the optimal position of the new paddle lead for each participant, following the procedures explained in Extended Data Fig. 4, but based on various model abstractions, as explained in the boxes above each prediction. **Step 4**, The optimal position of the new paddle lead was validated intraoperatively, as explained in Extended Data Fig. 4, and is shown on a CT scan reconstruction. The horizontal yellow line passing through the top electrodes of the paddle lead highlights the optimal position, thus allowing a direct comparison between the various predictions and the optimal position. The fully personalized models achieved the best performance.



Extended Data Fig. 6 | See next page for caption.